

On the Improvement of the Performance of Inexpensive Electromagnetic Skins by means of an Inverse Source Design Approach

G. Oliveri,⁽¹⁾⁽²⁾ *Fellow, IEEE*, F. Zardi,⁽¹⁾⁽²⁾ and A. Massa,⁽¹⁾⁽²⁾⁽³⁾⁽⁴⁾⁽⁵⁾ *Fellow, IEEE*

⁽¹⁾ *ELEDIA Research Center (ELEDIA@UniTN - University of Trento)*

DICAM - Department of Civil, Environmental, and Mechanical Engineering

Via Mesiano 77, 38123 Trento - Italy

E-mail: {giacomo.oliveri, francesco.zardi, andrea.massa}@unitn.it

Website: www.eledia.org/eledia-unitn

⁽²⁾ *CNIT - "University of Trento" ELEDIA Research Unit*

Via Sommarive 9, 38123 Trento - Italy

Website: www.eledia.org/eledia-unitn

⁽³⁾ *ELEDIA Research Center (ELEDIA@UESTC - UESTC)*

School of Electronic Science and Engineering, Chengdu 611731 - China

E-mail: andrea.massa@uestc.edu.cn

Website: www.eledia.org/eledia-uestc

⁽⁴⁾ *ELEDIA Research Center (ELEDIA@TSINGHUA - Tsinghua University)*

30 Shuangqing Rd, 100084 Haidian, Beijing - China

E-mail: andrea.massa@tsinghua.edu.cn

Website: www.eledia.org/eledia-tsinghua

⁽⁵⁾ *School of Electrical Engineering*

Tel Aviv University, Tel Aviv 69978 - Israel

E-mail: andrea.massa@eng.tau.ac.il

Website: <https://engineering.tau.ac.il/>

This work has been submitted to the IEEE for possible publication. Copyright may be transferred without notice, after which this version may no longer be accessible.

On the Improvement of the Performance of Inexpensive Electromagnetic Skins by means of an Inverse Source Design Approach

G. Oliveri, F. Zardi, and A. Massa

Abstract

A new methodology for the improvement of the performance of inexpensive static passive electromagnetic skins (*SP-EMSs*) is presented. The proposed approach leverages on the non-uniqueness of the inverse source problem associated to the *SP-EMS* design by decomposing the induced surface current into pre-image (*PI*) and null-space (*NS*) components. Successively, the unknown *EMS* layout and *NS* expansion coefficients are determined by means of an alternate minimization of a suitable cost function. This latter quantifies the mismatch between the ideal surface current, which radiates the user-defined target field, and that actually induced on the *EMS* layout. Results from a representative set of numerical experiments, concerned with the design of *EMSs* reflecting pencil-beam as well as contoured target patterns, are reported to assess the feasibility and the effectiveness of the proposed method in improving the performance of inexpensive *EMS* realizations. The measurements on an *EMS* prototype, featuring a conductive ink pattern printed on a standard paper substrate, are also shown to prove the reliability of the synthesis process.

Key words: Static Passive *EM* Skins; Smart Electromagnetic Environment; Next-Generation Communications; Metamaterials; Metasurfaces; Inverse Scattering; Non-Radiating Currents; Inverse Source Formulation.

1 Introduction and Motivation

The development of scalable and effective technologies for the implementation of the Smart Electromagnetic Environment (*SEME*) is a research area of growing relevance in next generation communication systems [1]-[7]. As a matter of fact, the possibility to tailor the electromagnetic propagation according to the wireless communication needs thanks to the *SEME* solutions has revealed potential significant improvements of the quality-of-service, the coverage, and the data throughput of current wireless systems [1][3]-[7]. In such a framework, static passive electromagnetic skins (*SP-EMSs*) have emerged as one of the most promising technological solutions thanks to the minimum costs and the maximum scalability [1][3][8]-[12].

An *SP-EMS* consists of a patterned artificial surface [13][14] that yields advanced field manipulation features by properly exploiting the geometrical/physical variations of its sub-wavelength meta-atoms [8]-[11]. By avoiding active/reconfigurable components and recurring to fabrication processes borrowed from traditional printed circuit board (*PCB*) technologies, a *SP-EMS* is typically less expensive than a reconfigurable intelligent surface (*RIS*), a smart repeater (*SR*), or an integrated access and backhaul (*IAB*) node [2][8]-[11]. Besides the cost, both the seamless installation and the absence of any power supply as well as the virtual transparency to wireless network operations have motivated a strong boost in the development, the demonstration, and the deployment of *SP-EMSs* [2][8]-[11].

However, several challenges have still to be addressed for enabling a mass production [2] and a large scale deployment of *SP-EMSs*. Indeed, the implementation of an inexpensive *SP-EMS* tens of meters wide requires much cheaper substrates than those currently adopted in *PCB* manufacturing. Moreover, single-layer meta-atoms with thin substrates would be much preferable owing to the smaller costs, an overall reduced weight, and a lower installation complexity. On the other hand, it is known from surface electromagnetics theory [13] that a single-layer meta-atom based on a low-quality substrate would typically result in a poor phase linearity and a sharp loss increase for some meta-atom configurations [e.g., see the design in Fig. 2(b)]. Thus, the arising *SP-EMS* would exhibit a mediocre power efficiency and a weak robustness to fabrication tolerances [13]. For this reason, current *SP-EMS* prototypes often feature standard *PCB* materials with non-negligible *per-meter* costs [8]-[12]. Therefore, there is a great interest in

demonstrating very inexpensive *SP-EMS*s still reaching a good efficiency.

To overcome, on the one hand, the issue of the costs associated to the use of standard *PCB* manufacturing in *SP-EMS* engineering, but also to avoid recurring to inexpensive *EMS*s with limited/poor performance, the inverse source (*IS*)-driven approach, which has recently-introduced in [10] to synthesize *SP-EMS*s complying with user-defined constraints, may be taken into account. More specifically, it has been proven that the non-uniqueness of the *EMS* design problem can be successfully exploited to synthesize multiple and equivalent (in terms of reflected footprint pattern) layouts so that (at least) one of those may fit user-defined requirements and goals [10]. In principle, such an approach is suitable for improving the efficiency of *SP-EMS*s based on inexpensive unit cells, but such an extension would require solving non-trivial issues such as how to (i) code the inexpensiveness constraint, (ii) apply and scale the generalized *IS*-method to wide *EMS*s, and (iii) yield inexpensive *SP-EMS*s still fulfilling the reflection requirements satisfied with their *PCB*-manufactured counterparts.

Therefore, a new approach is proposed hereinafter to improve the wave manipulation performance of *SP-EMS*s featuring inexpensive meta-atoms. By still leveraging on the non-uniqueness of the *IS* problem associated to the *SP-EMS* design, the induced surface current is first decomposed into pre-image (*PI*) and null-space (*NS*) components. Successively, the unknown *EMS* layout and *NS* expansion coefficients are determined by means of an alternate minimization of a suitable cost function. This latter quantifies the mismatch between the ideal surface current, which radiates the user-defined target field, and that induced on the *EMS* layout.

The main innovative contributions of this work with respect to the state of the art literature can be summarized in the following items:

- the generalization of the theoretical framework presented in [10] to the improvement of the performance of inexpensive *SP-EMS*s and, more in general, to the exploitation of the *NS* surface currents to synthesize *SP-EMS*s fulfilling user/application-driven requirements/constraints, but still with advanced field manipulation properties;
- the numerical assessment and the experimental proof of the feasibility of inexpensive *SP-EMS*s, not based on the traditional *PCB* technology and materials, affording user-defined footprint patterns that are typical of *SEME*s and (in general) next generation wireless

communication scenarios.

The outline of the paper is as follows. After the formulation of the *EMS* synthesis problem at hand (Sect. 2), the *IS NS*-based method for the optimized design of inexpensive *SP-EMS*s is detailed in Sect. 3. Section 4 reports the results of a representative set of numerical experiments to assess, also through an experimental validation, the effectiveness and the reliability of the proposed *EMS* synthesis method as well as the improved performance of the arising *SP-EMS* layouts. Finally, some conclusions and remarks are drawn (Sect. 5).

2 Design Problem Formulation

Let us consider the benchmark scenario in Fig. 1 where a planar *SP-EMS* located in the (x, y) plane is illuminated by an incident plane wave impinging from the angular direction $(\theta^{inc}, \varphi^{inc})$ whose associated electric field is [17][18]

$$\mathbf{E}^{inc}(\mathbf{r}) \triangleq (E_{TE}^{inc} \hat{\mathbf{e}}_{TE} + E_{TM}^{inc} \hat{\mathbf{e}}_{TM}) \exp(-j\mathbf{k}^{inc} \cdot \mathbf{r}) \quad (1)$$

where \mathbf{k}^{inc} is the incident wave vector

$$\begin{aligned} \mathbf{k}^{inc} \triangleq & -k_0 [\sin(\theta^{inc}) \cos(\varphi^{inc}) \hat{\mathbf{x}} + \\ & + \sin(\theta^{inc}) \sin(\varphi^{inc}) \hat{\mathbf{y}} + \cos(\theta^{inc}) \hat{\mathbf{z}}], \end{aligned} \quad (2)$$

while \mathbf{r} is the *EMS* local position vector [$\mathbf{r} = (x, y, z)$], k_0 and ζ_0 being the free-space wavenumber and the intrinsic impedance, respectively. Moreover, $\hat{\mathbf{e}}_{TE} = \frac{\mathbf{k}^{inc} \times \hat{\mathbf{z}}}{|\mathbf{k}^{inc} \times \hat{\mathbf{z}}|}$ and $\hat{\mathbf{e}}_{TM} = \frac{\hat{\mathbf{e}}_{TE} \times \mathbf{k}^{inc}}{|\hat{\mathbf{e}}_{TE} \times \mathbf{k}^{inc}|}$ are the *TE* and the *TM* mode unit vectors, respectively, while E_{TE}^{inc} and E_{TM}^{inc} are the corresponding complex-valued coefficients, $\hat{\mathbf{z}}$ is the normal to the skin surface, and $|\cdot|$ is the vector magnitude operator. The *SP-EMS* consists of $P \times Q$ meta-atoms centered at $\{\mathbf{r}_{pq} (p = 1, \dots, P; q = 1, \dots, Q)\}$ and it is univocally described by the descriptor vector \mathcal{D}

$$\mathcal{D} \triangleq \{d_{pq}; p = 1, \dots, P; q = 1, \dots, Q\}, \quad (3)$$

the (p, q) -th entry of which, d_{pq} ($p = 1, \dots, P; q = 1, \dots, Q$), is characterized by a set of L descriptors (i.e., $d_{pq} \triangleq \{d_{pq}^{(l)}; l = 1, \dots, L\}$).

The electromagnetic interactions between the incident field and the *SP-EMS* induce on the skin support Ω a surface electromagnetic current $\mathbf{J}(\mathbf{r}|\mathcal{D})$ ($\mathbf{J}(\mathbf{r}|\mathcal{D}) = J_x(\mathbf{r}|\mathcal{D})\hat{\mathbf{x}} + J_y(\mathbf{r}|\mathcal{D})\hat{\mathbf{y}}$) with electric and magnetic terms (i.e., $\mathbf{J}(\mathbf{r}|\mathcal{D}) \triangleq \hat{\mathbf{z}} \times [\zeta_0 \hat{\mathbf{z}} \times \mathbf{J}^e(\mathbf{r}'|\mathcal{D}) + \mathbf{J}^m(\mathbf{r}'|\mathcal{D})]$) that radiates in the far-field region Θ (i.e., $\mathbf{r} \in \Theta$) a reflected electric field given by

$$\mathbf{E}^{refl}(\mathbf{r}|\mathcal{D}) = \frac{jk_0}{4\pi} \frac{\exp(-jk_0 r)}{r} \int_{\Omega} \mathbf{J}(\mathbf{r}'|\mathcal{D}) \exp(jk_0 \hat{\mathbf{r}} \cdot \mathbf{r}') d\mathbf{r}'. \quad (4)$$

The relation among the the electric/magnetic terms of the induced current and the *SP-EMS* unit cell descriptors \underline{d}_{pq} ($p = 1, \dots, P, q = 1, \dots, Q$) can be expressed according to the Love's equivalence principle [13][8] as follows

$$\begin{cases} \mathbf{J}^e(\mathbf{r}|\mathcal{D}) = \frac{1}{\zeta_0} \hat{\mathbf{z}} \times \mathbf{k}^{inc} \times \underline{\underline{\Gamma}}(\mathbf{r}|\mathcal{D}, \mathbf{k}^{inc}) \cdot \mathbf{E}^{inc}(\mathbf{r}) \\ \mathbf{J}^m(\mathbf{r}|\mathcal{D}) = -\hat{\mathbf{z}} \times \underline{\underline{\Gamma}}(\mathbf{r}|\mathcal{D}, \mathbf{k}^{inc}) \cdot \mathbf{E}^{inc}(\mathbf{r}) \end{cases} \quad (5)$$

where

$$\underline{\underline{\Gamma}}(\mathbf{r}|\mathcal{D}, \mathbf{k}^{inc}) = \begin{bmatrix} \Gamma_{TE}(\mathbf{r}|\mathcal{D}, \mathbf{k}^{inc}) & 0 \\ 0 & \Gamma_{TM}(\mathbf{r}|\mathcal{D}, \mathbf{k}^{inc}) \end{bmatrix} \quad (6)$$

is the local complex reflection matrix of an *SP-EMS* with descriptors \mathcal{D} .

Under the local periodicity assumption, it turns out that [13]

$$\underline{\underline{\Gamma}}(\mathbf{r}|\mathcal{D}, \mathbf{k}^{inc}) \approx \sum_{p=1}^P \sum_{q=1}^Q \underline{\underline{\Gamma}}(\underline{d}_{pq}, \mathbf{k}^{inc}) \Pi^{pq}(\mathbf{r}) \quad (7)$$

where $\Pi_{pq}(\mathbf{r})$ is the (p, q) -th ($p = 1, \dots, P; q = 1, \dots, Q$) pixel basis function centered in \mathbf{r}_{pq} ($\mathbf{r}_{pq} \in \Omega$), while the local reflection coefficient for a given meta-atom featuring \underline{d} and illuminated by an incident plane wave with an incident wave vector \mathbf{k}^{inc} , $\underline{\underline{\Gamma}}(\underline{d}, \mathbf{k}^{inc})$, can be computed with analytical, numerical, hybrid, or artificial intelligence-based methods [13][19][20]. In this paper, a full-wave commercial *SW* [21] has been used to build a database \mathbb{D} with entries $\{(\underline{d}, \mathbf{k}^{inc}), \underline{\underline{\Gamma}}(\underline{d}, \mathbf{k}^{inc})\}$.

Within the *IS* framework [10], a basic formulation of the *SP-EMS* synthesis problem can be then stated as follows

Standard *SP-EMS IS* Problem (SISP) - Given an incident field $\mathbf{E}^{inc}(\mathbf{r})$ ($\mathbf{r} \in \Omega$),

a desired reflected field $\tilde{\mathbf{E}}^{refl}(\mathbf{r})$ ($\mathbf{r} \in \Theta$), which corresponds to the *pre-image* surface current $\mathbf{J}_{PI}(\mathbf{r})$ ($\mathbf{r} \in \Omega$) fulfilling the source-version of (4)

$$\tilde{\mathbf{E}}^{refl}(\mathbf{r}) = \frac{jk_0 \exp(-jk_0 r)}{4\pi r} \int_{\Omega} \tilde{\mathbf{J}}(\mathbf{r}') \exp(jk_0 \hat{\mathbf{r}} \cdot \mathbf{r}') d\mathbf{r}' \quad (8)$$

($\mathbf{J}_{PI} \rightarrow \tilde{\mathbf{J}}$), and a meta-atom featuring a local reflection coefficient $\underline{\Gamma}(\underline{d}, \mathbf{k}^{inc})$, find the descriptors of the *SP-EMS* \mathcal{D}^{opt} such that

$$\Phi(\mathcal{D}) = \frac{\int_{\Omega} |\mathbf{J}(\mathbf{r}'|\mathcal{D}) - \mathbf{J}_{PI}(\mathbf{r}')|^2 d\mathbf{r}'}{\int_{\Omega} |\mathbf{J}_{PI}(\mathbf{r}')|^2 d\mathbf{r}'} \quad (9)$$

is minimized (i.e., $\mathcal{D}^{opt} = \arg\{\min_{\mathcal{D}}[\Phi(\mathcal{D})]\}$).

Unfortunately, there is not guarantee that \mathcal{D}^{opt} yields a good matching between induced, $\mathbf{J}(\mathbf{r}|\mathcal{D}^{opt})$, and pre-image, $\mathbf{J}_{PI}(\mathbf{r})$, currents (i.e., $\Phi(\mathcal{D}) \rightarrow 0$), especially if inexpensive and thin substrates are at hand. Fortunately, it is known that *IS* problems are ill-posed and their solutions are not unique. This is the case of computing the surface current radiating the desired field $\tilde{\mathbf{E}}^{refl}(\mathbf{r})$ ($\mathbf{r} \in \Theta$), thus $\mathbf{J}_{PI}(\mathbf{r})$ is just one of the infinite set of solutions of (8). Indeed, the surface current

$$\tilde{\mathbf{J}}(\mathbf{r}) = \mathbf{J}_{PI}(\mathbf{r}) + \mathbf{J}_{NS}(\mathbf{r}), \quad (10)$$

where $\mathbf{J}_{NS}(\mathbf{r})$ is the *null-space* surface current that satisfies the condition

$$\mathbf{0} = \frac{jk_0 \exp(-jk_0 r)}{4\pi r} \int_{\Omega} \mathbf{J}_{NS}(\mathbf{r}') \exp(jk_0 \hat{\mathbf{r}} \cdot \mathbf{r}') d\mathbf{r}', \quad (11)$$

still radiates the target distribution $\tilde{\mathbf{E}}^{refl}(\mathbf{r})$ ($\mathbf{r} \in \Theta$).

Accordingly, the original *SISP* can be reformulated as follows

Low-Complexity SP-EMS IS Problem (LISP) - Given an incident field $\mathbf{E}^{inc}(\mathbf{r})$ ($\mathbf{r} \in \Omega$), a desired reflected field $\tilde{\mathbf{E}}^{refl}(\mathbf{r})$ ($\mathbf{r} \in \Theta$), and a meta-atom featuring a local reflection coefficient $\underline{\Gamma}(\underline{d}, \mathbf{k}^{inc})$, find the descriptors of the *SP-EMS* \mathcal{D}^{opt} and

the most suitable null-space surface current $\mathbf{J}_{NS}^{opt}(\mathbf{r})$ ($\mathbf{r} \in \Omega$) such that

$$\Phi(\mathcal{D}, \mathbf{J}_{NS}(\mathbf{r})) = \frac{\int_{\Omega} |\mathbf{J}(\mathbf{r}'|\mathcal{D}) - [\mathbf{J}_{PI}(\mathbf{r}') + \mathbf{J}_{NS}(\mathbf{r}')]|^2 d\mathbf{r}'}{\int_{\Omega} |\mathbf{J}_{PI}(\mathbf{r}') + \mathbf{J}_{NS}(\mathbf{r}')|^2 d\mathbf{r}'} \quad (12)$$

is minimized (i.e., $(\mathcal{D}^{opt}, \mathbf{J}_{NS}^{opt}(\mathbf{r})) = \arg \{ \min_{(\mathcal{D}, \mathbf{J}_{NS}(\mathbf{r}))} [\Phi(\mathcal{D}, \mathbf{J}_{NS}(\mathbf{r}))] \}$).

3 Solution Procedure

In order to solve the *LISP*, let us first perform the *SVD* [22] of the linear operator \mathcal{L} in (11) (i.e.,

$$\mathcal{L} : \tilde{\mathbf{J}} \rightarrow \tilde{\mathbf{E}}^{refl} \text{ being } \mathcal{L}(\cdot) \triangleq \int_{\Omega} (\cdot) \frac{jk_0 \exp[jk_0(\hat{\mathbf{r}} \cdot \mathbf{r}' - r)]}{4\pi r} d\mathbf{r}'$$

$$\mathcal{L}(\tilde{\mathbf{J}})(\mathbf{r}) = \sum_{s=1}^S \sigma_s U_s(\mathbf{r}) \int_{\Omega} \tilde{\mathbf{J}}(\mathbf{r}') V_s^*(\mathbf{r}') d\mathbf{r}' \quad \mathbf{r} \in \Theta, \quad (13)$$

where σ_s is the s -th ($s = 1, \dots, S$) singular value of $\mathcal{L}(\cdot)$ with the ordering $\sigma_{s-1} \geq \sigma_s \geq \sigma_{s+1}$ and $\sigma_S \rightarrow 0$ for $S \rightarrow \infty$, while U_s and V_s are orthogonal normalized basis eigenfunctions in the reflected field ($U_s(\mathbf{r}) \in \mathfrak{S} \{ \tilde{\mathbf{E}}^{refl}(\mathbf{r}); \mathbf{r} \in \Theta \}$) and the surface current ($V_s(\mathbf{r}) \in \mathfrak{S} \{ \tilde{\mathbf{J}}(\mathbf{r}); \mathbf{r} \in \Omega \}$) spaces, respectively, $*$ being the adjoint operator. Therefore, the surface current $\tilde{\mathbf{J}}(\mathbf{r})$ ($\mathbf{r} \in \Omega$) (10) can be expanded in terms of singular values and current eigenfunctions as follows

$$\mathbf{J}_{PI}(\mathbf{r}) = \sum_{s=1}^{s_{th}} \frac{1}{\sigma_s} V_s(\mathbf{r}) \int_{\Theta} \tilde{\mathbf{E}}^{refl}(\mathbf{r}') U_s^*(\mathbf{r}') d\mathbf{r}' \quad \mathbf{r} \in \Omega, \quad (14)$$

$$\mathbf{J}_{NS}(\mathbf{r}|\underline{\beta}) = \sum_{s=s_{th}+1}^S \beta_s V_s(\mathbf{r}) \quad \mathbf{r} \in \Omega, \quad (15)$$

where s_{th} is the *SVD* truncation index ($s_{th} \triangleq \arg \left[\min_s \left(\frac{\sigma_s}{\sigma_1} \geq \eta_{SVD} \right) \right]$, η_{SVD} being a user-defined threshold) and β_s is the s -th ($s = 1, \dots, S$) arbitrary null-space coefficient. It is worthwhile pointing out that $\mathcal{L}(\mathbf{J}_{NS})(\mathbf{r}) = 0$ (11) whatever the set of β_s coefficients, $\underline{\beta} = \{\beta_s; s > s_{th}\}$, since the set $\{V_s(\mathbf{r}); s > s_{th}\}$ belongs to the kernel of the operator $\mathcal{L}(\cdot)$.

Thanks to (15), the *LISP* is then reformulated in the following alternative manner:

LISP (SVD-Based Formulation) - Given an incident field $\mathbf{E}^{inc}(\mathbf{r})$ ($\mathbf{r} \in \Omega$), a desired reflected field $\tilde{\mathbf{E}}^{refl}(\mathbf{r})$ ($\mathbf{r} \in \Theta$), a meta-atom featuring a local reflection coefficient

$\underline{\underline{\Gamma}}(\underline{d}, \mathbf{k}^{inc})$, and the *SVD* threshold η_{SVD} , find the descriptors of the *SP-EMS* \mathcal{D}^{opt} and the most suitable set of null-space coefficients $\underline{\underline{\beta}}^{opt}$ such that

$$\Phi(\mathcal{D}, \underline{\underline{\beta}}) = \frac{\int_{\Omega} \left| \mathbf{J}(\mathbf{r}'' | \mathcal{D}) - \tilde{\mathbf{J}}(\mathbf{r}'' | \underline{\underline{\beta}}) \right|^2 d\mathbf{r}''}{\int_{\Omega} \left| \tilde{\mathbf{J}}(\mathbf{r}'' | \underline{\underline{\beta}}) \right|^2 d\mathbf{r}''} \quad (16)$$

is minimized (i.e., $(\mathcal{D}^{opt}, \underline{\underline{\beta}}^{opt}) = \arg \left\{ \min_{(\mathcal{D}, \underline{\underline{\beta}})} [\Phi(\mathcal{D}, \underline{\underline{\beta}})] \right\}$) being

$$\tilde{\mathbf{J}}(\mathbf{r} | \underline{\underline{\beta}}) = \sum_{s=1}^{sth} \frac{1}{\sigma_s} V_s(\mathbf{r}) \int_{\Theta} \tilde{\mathbf{E}}^{refl}(\mathbf{r}') U_s^*(\mathbf{r}') d\mathbf{r}' + \sum_{s=sth+1}^S \beta_s V_s(\mathbf{r}). \quad (17)$$

In order to minimize (16), while a simultaneous optimization of the two unknowns (i.e., \mathcal{D} and $\underline{\underline{\beta}}$) is in principle viable, an alternate optimization significantly simplifies the search of \mathcal{D}^{opt} and $\underline{\underline{\beta}}^{opt}$ [23]. Such a strategy can be summarized into the interleaving of two phases aimed at updating the sequences $\{\mathcal{D}_n; n = 1, \dots, N\}$ and $\{\underline{\underline{\beta}}_n; n = 1, \dots, N\}$ towards $\mathcal{D}_n \rightarrow \mathcal{D}^{opt}$ and $\underline{\underline{\beta}}_n \rightarrow \underline{\underline{\beta}}^{opt}$, n ($n = 1, \dots, N$) being the updating index.

The former (“*SP-EMS Update*”) generates the n -th ($n = 1, \dots, N$) *SP-EMS* trial layout \mathcal{D}_n by minimizing the cost function $\Phi_{\beta}(\mathcal{D})$ given by $\Phi_{\beta}(\mathcal{D}) \triangleq \Phi(\mathcal{D}, \underline{\underline{\beta}}_{n-1})$ (i.e., $\mathcal{D}_n = \arg \left\{ \min_{\mathcal{D}} [\Phi(\mathcal{D}, \underline{\underline{\beta}}_{n-1})] \right\}$) being $\underline{\underline{\beta}}_0 = \underline{\underline{0}}$ by means of an exhaustive search within the off-line built database \mathbb{D} . More in detail, for each (p, q) -th ($p = 1, \dots, P; q = 1, \dots, Q$) meta-atom of the *EMS* - given the incident field at hand ($\rightarrow \mathbf{k}^{inc}$) - the exhaustive process identifies in \mathbb{D} the value $\underline{d}_{pq}|_n$ (i.e., the most suitable entry $\{(\underline{d}_{pq}|_n, \mathbf{k}^{inc}), \underline{\underline{\Gamma}}(\underline{d}_{pq}|_n, \mathbf{k}^{inc})\}$) for which $\mathbf{J}(\mathbf{r}_{pq} | \underline{d}_{pq}|_n) \approx \tilde{\mathbf{J}}(\mathbf{r}_{pq} | \underline{\underline{\beta}}_{n-1})$ being $\mathbf{J}(\mathbf{r}_{pq} | \underline{d}_{pq}) = \hat{\mathbf{z}} \times [\zeta_0 \hat{\mathbf{z}} \times \frac{1}{\eta} \hat{\mathbf{z}} \times \mathbf{k}^{inc} \times \underline{\underline{\Gamma}}(\underline{d}_{pq}, \mathbf{k}^{inc}) \Pi^{pq}(\mathbf{r}) \cdot \mathbf{E}^{inc}(\mathbf{r}) - \hat{\mathbf{z}} \times \underline{\underline{\Gamma}}(\underline{d}_{pq}, \mathbf{k}^{inc}) \Pi^{pq}(\mathbf{r}) \cdot \mathbf{E}^{inc}(\mathbf{r})]$ (Sect. 2).

The second phase (“*NS Current Update*”) yields the n -th ($n = 1, \dots, N$) set of null-space coefficients $\underline{\underline{\beta}}_n$ by minimizing the cost function $\Phi_{\mathcal{D}}(\underline{\underline{\beta}})$ given by $\Phi_{\mathcal{D}}(\underline{\underline{\beta}}) \triangleq \Phi(\mathcal{D}_n, \underline{\underline{\beta}})$ (i.e., $\underline{\underline{\beta}}_n = \arg \left\{ \min_{\underline{\underline{\beta}}} [\Phi(\mathcal{D}_n, \underline{\underline{\beta}})] \right\}$) with a multi-agent evolutionary optimization technique based on the particle swarm mechanisms [15]. The nested loop is terminated if either $n = N$ or $\Phi_{\beta}(\mathcal{D}_n) \leq \eta_{\Phi}$ or $\Phi_{\mathcal{D}}(\underline{\underline{\beta}}_n) \leq \eta_{\Phi}$ (η_{Φ} being the convergence threshold) by outputting the optimal setups $\mathcal{D}^{opt} = \mathcal{D}_n$ and $\underline{\underline{\beta}}^{opt} = \underline{\underline{\beta}}_n$.

4 Numerical Results and Experimental Validation

This section is aimed at assessing the effectiveness of the *SP-EMS* design strategy presented in Sect. 3 for solving the problem formulated in Sect. 2 with a selected set of numerical results (Sect. 4.1) and an experimental validation (Sect. 4.2).

Without loss of generality, the following benchmark scenario has been assumed. The primary far-field source has been modeled with a plane wave at $f = 5.5$ [GHz] impinging on the *SP-EMS* from the broadside direction (i.e., $\theta^{inc} = \varphi^{inc} = 0$ [deg]) with a linearly polarized *TE* field of unitary magnitude (i.e., $E_{TE}^{inc} = 1$ [V/m] and $E_{TM}^{inc} = 0$ [V/m]) and incident wave vector $\mathbf{k}^{inc} = -k_0 \hat{\mathbf{z}}$. The control parameters in Sect. 3 have been set to $\eta_{SVD} = 10^{-1}$, $\eta_\Phi = 10^{-4}$, and $N = 10^4$. Moreover, the field pattern reflected from the *SP-EMS* \mathcal{D} (i.e., $\mathbf{E}^{refl}(\mathbf{r}|\mathcal{D})$, $\mathbf{r} \in \Theta$) has been simulated with the commercial software Ansys HFSS [21] in a set of M sampling points [$\rightarrow S = \min(P \times Q, M)$].

A basic unit cell geometry Δ -sided featuring a conductive-ink square patch [i.e., $L = 1$ - Fig. 2(a)] printed on single-layer *paper substrate* [16][24] has been chosen as a representative example of a very inexpensive meta-atom. Such a choice has been motivated by the potential reduction of the manufacturing costs (i.e., two orders of magnitude lower than traditional *PCB* technology [24]) as well as its suitability for a fast and ultra-low-cost mass production [16]. According to the guidelines in [16], the paper substrate has been modeled with a homogeneous layer having a relative permittivity of $\varepsilon_r = 3.2$ and a dielectric loss tangent equal to $\tan \delta = 7.7 \times 10^{-2}$ with thickness $\tau = 2.08 \times 10^{-3}$ [m]. Such a setup is not a customized one since similar values model different types of paper/cardboard in sub-6 GHz applications [25]-[27].

The magnitude [Fig. 2(b)] and the phase [Fig. 2(c)] of the reflection coefficient, $\Gamma_{TE}(d^{(1)})$, as a function of the patch side $d^{(1)}$ of the meta-atom in Fig. 2(a) have been numerically simulated by assuming a 0.5λ wide unit cell and a printing precision of 10^{-4} [m], which faithfully models a typical office inkjet printer with a resolution of 1200 dots-per-inch. As expected, owing to the high-loss substrate material besides the single-layer nature of the meta-atom, the magnitude of the reflection coefficient is poor at some values of $d^{(1)}$. For instance, $|\Gamma_{TE}(d^{(1)})|_{d^{(1)} \approx 1.4 \times 10^{-3} [m]} \approx -23.5$ [dB] [Fig. 2(b)]. Such a value is much worse than that of typical *PCB*-based meta-atoms even though printed on relatively inexpensive substrates

[13][8][9]. For comparison purposes, let us consider the case of a meta-atom printed on an ISOLA 370HR substrate ($\epsilon_r = 3.92$, $\tan \delta = 2.5 \times 10^{-2}$, and $\tau = 7.11 \times 10^{-4}$ [m]), plotted with the blue line in Figs. 2(b)-2(c), where $|\Gamma_{TE}(d^{(1)})| \geq -11.7$ [dB] [Fig. 2(b)].

4.1 Numerical Assessment

The first test case deals with a $P \times Q = 35 \times 35$ *SP-EMS* centered at $h = 5$ [m] over the floor [Fig. 1(a)] within an area of $A_\Omega \approx 0.95 \times 0.95$ [m²]. Such a skin has been requested to reflect in the coverage area Θ of extension $A_\Theta \approx 0.95 \times 0.95$ [m²] the target field distribution $\tilde{\mathbf{E}}^{refl}(\mathbf{r})$ ($\mathbf{r} \in \Theta$) in Fig. 3(a), which consists of a pencil beam focused towards the direction $(\theta^{refl}, \varphi^{refl}) = (30, -45)$ [deg].

According to the design procedure in Sect. 3, the synthesis process starts with the *SVD* [22] of the linear operator \mathcal{L} in (11) to determine the S singular values $\{\sigma_s; s = 1, \dots, S\}$ and the corresponding sets of eigenfunctions, $\{U_s(\mathbf{r}) (\mathbf{r} \in \Theta); s = 1, \dots, S\}$ and $\{V_s(\mathbf{r}) (\mathbf{r} \in \Omega); s = 1, \dots, S\}$ so that the known terms in (17) are defined and the unknowns in (16) to be optimized are \mathcal{D} and $\underline{\beta}$. The plot of the normalized \mathcal{L} spectrum (i.e., $\{\hat{\sigma}_s; s = 1, \dots, S\}$ being $\hat{\sigma}_s \triangleq \frac{\sigma_s}{\sigma_1}$) in Fig. 3(b) exhibits the well-known “knee” behaviour and the number of singular values above the threshold η_{SVD} turns out to be approximately $s_{th} \approx 335$.

Figure 4 shows the null-space coefficients $\underline{\beta}^{opt}$ and the *SP-EMS* layout \mathcal{D}^{opt} synthesized at the converge ($n = N$) of the optimization process to minimize (16) (Sect. 3), while the field reflected by the *SP-EMS* in the far-field region Θ , $\mathbf{E}^{refl}(\mathbf{r}|\mathcal{D})$ ($\mathbf{r} \in \Theta$), is given in Fig. 5(a). This latter distribution turns out to be quite close to the target one $\tilde{\mathbf{E}}^{refl}(\mathbf{r})$ ($\mathbf{r} \in \Theta$) [Fig. 3(a)] with a faithful generation of the pencil beam along the right angular direction $(\theta^{refl}, \varphi^{refl}) = (30, -45)$ [deg].

In order to detail the features of the *NS*-based *SP-EMS* synthesis, let us analyze the behaviour of the null-space coefficients $\underline{\beta}^{opt}$ and related quantities [i.e., $\tilde{\mathbf{J}}(\mathbf{r}|\underline{\beta})$ and $\mathbf{J}_{NS}(\mathbf{r}|\underline{\beta})$ ($\mathbf{r} \in \Omega$)] together with the corresponding footprint fields [Figs. 5(c)-5(d)]. As expected from *IS* theory [10], there exist a *NS* current $\mathbf{J}_{NS}(\mathbf{r}|\underline{\beta})$ ($\mathbf{r} \in \Omega$) [Figs. 6(c)-6(d)] corresponding to the non-zero magnitude entries of $\underline{\beta}^{opt}$ [Fig. 4(a)] that, by definition, radiates in far-field the null field $\mathbf{E}_{NS}^{refl}(\mathbf{r}|\underline{\beta})$ ($\mathbf{r} \in \Theta$) [Fig. 5(c)] and that, when superimposed to the *PI* current term in Fig.

6(a)-6(b) [i.e., $\tilde{\mathbf{J}}(\mathbf{r}|\underline{\beta}) = \mathbf{J}_{PI}(\mathbf{r}|\underline{\beta}) + \mathbf{J}_{NS}(\mathbf{r}|\underline{\beta})$ ($\mathbf{r} \in \Omega$) - Figs. 6(e)-6(f)], does not perturb the *PI* footprint [i.e., $\mathbf{E}_{TOT}^{refl}(\mathbf{r}|\underline{\beta}) \approx \mathbf{E}_{PI}^{refl}(\mathbf{r}|\underline{\beta})$ ($\mathbf{r} \in \Theta$) - Fig. 5(d) vs. Fig. 5(b)], this latter being a close approximation of the target one [i.e., $\mathbf{E}_{PI}^{refl}(\mathbf{r}|\underline{\beta}) \approx \tilde{\mathbf{E}}^{refl}(\mathbf{r})$ ($\mathbf{r} \in \Theta$) - Fig. 5(b) vs. Fig. 3(a)] owing to (14). Still concerning the synthesized $\underline{\beta}^{opt}$ vector, it is worth observing the highly-irregular phase profile in Fig. 4(a), which is somehow generally *a-priori* unpredictable. This is a further motivation for choosing in Sect. 3 a global optimizer to minimize the cost function $\Phi_{\mathcal{D}}(\underline{\beta})$, besides the need of facing the nonlinear nature of this latter.

Next, let us complete the discussion on the features of the *NS*-based approach by focusing on \mathcal{D}^{opt} in comparison with \mathcal{D}^{PI} , which are the *SP-EMS* descriptors yielded by just matching the *PI* currents in (16) (i.e., $\mathcal{D}^{PI} = \mathcal{D}_1$ where $\mathcal{D}_1 = \arg \left\{ \min_{\mathcal{D}} \left[\Phi \left(\mathcal{D}, \underline{\beta}_0 \right) \right] \right\}$ being $\underline{\beta}_0 = \underline{\mathbf{0}}$), thus neglecting the *NS* contribution. Figure 7 shows the layout of the \mathcal{D}^{PI} -coded *SP-EMS* [Fig. 7(a)] and the corresponding reflected footprint $\mathbf{E}^{refl}(\mathbf{r}|\mathcal{D}^{PI})$ ($\mathbf{r} \in \Theta$) [Fig. 7(b)]. In order to highlight the improvement granted by the exploitation of the *NS* contribution, Figure 7(c) shows the map of the local power improvement index $\mathcal{P}_{\mathcal{D}'\mathcal{D}''}(\mathbf{r})$,

$$\mathcal{P}_{\mathcal{D}'\mathcal{D}''}(\mathbf{r}) \triangleq \frac{\left[|\mathbf{E}^{refl}(\mathbf{r}|\mathcal{D}')|^2 - |\mathbf{E}^{refl}(\mathbf{r}|\mathcal{D}'')|^2 \right]}{\max_{\mathbf{r} \in \Theta} \left\{ |\mathbf{E}^{refl}(\mathbf{r}|\mathcal{D}'')|^2 \right\}}, \quad (18)$$

of \mathcal{D}^{opt} ($\mathcal{D}' \leftarrow \mathcal{D}^{opt}$) vs. \mathcal{D}^{PI} ($\mathcal{D}'' \leftarrow \mathcal{D}^{PI}$) in the far-field region Θ ($\mathbf{r} \in \Theta$). One can infer that there is a peak power improvement exactly along the target direction (i.e., $\theta_{max} = \theta^{refl}$, $\theta_{max} \triangleq \arg \left\{ \max_{\mathbf{r} \in \Theta} [\mathcal{P}_{\mathcal{D}^{opt}\mathcal{D}^{PI}}(\mathbf{r})] \right\}$), which amounts to $\mathcal{P}_{max} \triangleq \max_{\mathbf{r} \in \Theta} [\mathcal{P}_{\mathcal{D}^{opt}\mathcal{D}^{PI}}(\mathbf{r})] \approx 28$ %, that has been yielded without making the *SP-EMS* architecture more complex (e.g., multi-layered) or using more expensive materials, but just exploiting the non-uniqueness of the *IS* problem at hand.

The last study carried out on the first test case has been devoted to assess the effectiveness of the proposed *SP-EMS* synthesis approach in overcoming the intrinsic limitations of inexpensive substrates (e.g., here a paper substrate) to reach performance closer to those of circuit-graded materials. Towards this end, a *PI*-based *SP-EMS* has been synthesized using an ISOLA substrate [$\mathcal{D} = \mathcal{D}_{ISOLA}^{PI}$ - Fig. 8(a)] and the resulting footprint pattern $\mathbf{E}^{refl}(\mathbf{r}|\mathcal{D}_{ISOLA}^{PI})$ ($\mathbf{r} \in \Theta$) [Fig. 8(b)] has been compared with those in Fig. 7(b) [i.e., $\mathbf{E}^{refl}(\mathbf{r}|\mathcal{D}_{paper}^{PI})$ ($\mathbf{r} \in \Theta$)] and Fig.

5(a) [i.e., $\mathbf{E}^{refl}(\mathbf{r}|\mathcal{D}_{paper}^{opt})$ ($\mathbf{r} \in \Theta$)]. More specifically, the plots of the reflected fields in the $\varphi^{refl} = -45$ [deg] cut are reported in Fig. 9(a). As it can be noticed, the power focusing efficiency of the *NS*-based paper-printed layout turns out to be closer to that from the *PI*-based ISOLA one [e.g., $\Delta\mathbf{E}_{\mathcal{D}_{ISOLA}^{PI}\mathcal{D}_{paper}^{opt}}^{refl}(\theta^{refl}, \varphi^{refl}) \approx 1.8$ [dB] vs. $\Delta\mathbf{E}_{\mathcal{D}_{ISOLA}^{PI}\mathcal{D}_{paper}^{PI}}^{refl}(\theta^{refl}, \varphi^{refl}) \approx 2.9$ [dB] being $\Delta\mathbf{E}_{\mathcal{D}'\mathcal{D}''}^{refl}(\theta, \varphi) \triangleq \frac{|\mathbf{E}^{refl}(\theta, \varphi|\mathcal{D}')|}{|\mathbf{E}^{refl}(\theta, \varphi|\mathcal{D}'')|}$ - see the inset in Fig. 9(a)]. Moreover, the $\mathcal{D}_{paper}^{opt}$ -layout improves the sidelobe control of its *PI* counterpart (e.g., $\Delta\mathbf{E}_{\mathcal{D}_{paper}^{PI}\mathcal{D}_{paper}^{opt}}^{refl}(\theta, \varphi^{refl}) \Big|_{\theta=0 [deg]} \approx 2.1$ [dB] and $\Delta\mathbf{E}_{\mathcal{D}_{paper}^{PI}\mathcal{D}_{paper}^{opt}}^{refl}(\theta, \varphi^{refl}) \Big|_{\theta=82 [deg]} \approx 2.98$ [dB]), while it performs analogously or better than the \mathcal{D}_{ISOLA}^{PI} one (e.g., $\Delta\mathbf{E}_{\mathcal{D}_{ISOLA}^{PI}\mathcal{D}_{paper}^{opt}}^{refl}(\theta, \varphi^{refl}) \Big|_{\theta=0 [deg]} \approx 0.7$ [dB] and $\Delta\mathbf{E}_{\mathcal{D}_{ISOLA}^{PI}\mathcal{D}_{paper}^{opt}}^{refl}(\theta, \varphi^{refl}) \approx 0.2$ [dB]). For completeness, the maps of the local power improvement index $\mathcal{P}(\mathbf{r})$ [$\mathcal{P}_{\mathcal{D}_{paper}^{PI}\mathcal{D}_{ISOLA}^{PI}}(\mathbf{r})$ - Fig. 9(b); $\mathcal{P}_{\mathcal{D}_{paper}^{opt}\mathcal{D}_{ISOLA}^{PI}}(\mathbf{r})$ - Fig. 9(c)] are reported, as well.

The second set of numerical experiments has been aimed at evaluating the effectiveness of the *NS*-based *EMS* synthesis when varying the Ω size. More specifically, the same scenario of the previous test case has been considered, but the number of unit cells of the square (i.e., $P = Q$) *SP-EMS* has been changed from $P = 15$ ($\rightarrow A_{\Omega} \approx 0.16$ [m²]) up to $P = 95$ ($\rightarrow A_{\Omega} \approx 6.7$ [m²]). The plot of \mathcal{P}_{max} versus the *EMS* aperture in Fig. 10(a) confirms the enhancement of the maximum value of the reflection efficiency, still along θ^{refl} since always $\theta_{max} = \theta^{refl}$, with respect to the *PI* solution regardless of the *EMS* size (i.e., $\mathcal{P}_{max} > 0$ %). However, one can notice that the achievable improvement is more significant for smaller apertures (e.g., $\mathcal{P}_{max}|_{P=95} = 3$ % vs. $\mathcal{P}_{max}|_{P=35} = 28$ % vs. $\mathcal{P}_{max}|_{P=15} = 38$ %). This is a key outcome towards the implementation of wide inexpensive and high-efficiency *SP-EMS*s since it would suggest the designer to avoid monolithic realizations, while preferring the modular ones [29] leveraging on small tiles for covering the *EMS* aperture.

For illustrative purposes, Figure 10(b) shows the plots of the reflected field $\mathbf{E}^{refl}(\theta, \varphi^{refl}|\mathcal{D})$ along the cut at $\varphi^{refl} = -45$ [deg] (-90 [deg] $\leq \theta \leq 90$ [deg]) for two representative *EMS* sizes (i.e., $P = 15$ and $P = 55$). Quantitatively, the advantage of exploiting a *NS*-driven design in terms of power focusing efficiency reduces from $\Delta\mathbf{E}_{\mathcal{D}_{opt}\mathcal{D}_{PI}}^{refl}(\theta^{refl}, \varphi^{refl}) \Big|_{P=Q=15} \approx 1.4$ [dB] down to $\Delta\mathbf{E}_{\mathcal{D}_{opt}\mathcal{D}_{PI}}^{refl}(\theta^{refl}, \varphi^{refl}) \Big|_{P=Q=55} \approx 0.5$ [dB]. The same behavior holds true for the sidelobe control since at the first sidelobe position ($\theta = 0$ [deg]) it turns out that $\Delta\mathbf{E}_{\mathcal{D}_{opt}\mathcal{D}_{PI}}^{refl}(0, \varphi^{refl}) \Big|_{P=Q=15} \approx 3.6$ [dB] vs. $\Delta\mathbf{E}_{\mathcal{D}_{opt}\mathcal{D}_{PI}}^{refl}(0, \varphi^{refl}) \Big|_{P=Q=55} \approx 1.3$ [dB], while

at the second one ($\theta = 78$ [deg] when $P = 15$ and $\theta = 84.4$ [deg] when $P = 55$) the values are $\Delta \mathbf{E}_{\mathcal{D}^{opt}\mathcal{D}^{PI}}^{refl} (78, \varphi^{refl}) \Big|_{P=Q=15} \approx 4.1$ [dB] vs. $\Delta \mathbf{E}_{\mathcal{D}^{opt}\mathcal{D}^{PI}}^{refl} (84.4, \varphi^{refl}) \Big|_{P=Q=55} \approx 0.8$ [dB].

The third numerical assessment is concerned with the dependence of the *EMS* synthesis results on the target reflection direction. Towards this end, an analysis on a square *EMS* with $P = Q = 35$ atoms affording a pencil beam in the azimuth plane $\varphi^{refl} = -45$ [deg] and along the variable elevation θ^{refl} (20 [deg] $\leq \theta^{refl} \leq 50$ [deg]) has been carried out. The outcomes are summarized in Fig. 11 where the dependence of \mathcal{P}_{\max} on the scan direction is shown. One can observe that the power efficiency improvement granted by the proposed approach is non-negligible ($\mathcal{P}_{\max}|_{\theta^{refl}} > 24.5$ [dB]) also at the wider scan angles (e.g., $\mathcal{P}_{\max}|_{\theta^{refl}=50 \text{ [deg]}} \approx 24.7$ [dB]), when the use of poor/inexpensive substrates becomes more and more critical, and the maximum range of variation of \mathcal{P}_{\max} amounts to ~ 3 [dB] within the angular range under test.

The last set of numerical experiments deals with more complex coverage tasks. Indeed, the reflected pattern has been required to comply with a contoured footprint modeling a realistic operative scenario (“Gare du Nord - Paris” - Fig. 12) instead of focusing in a target direction like in the previous pencil beam test cases. More in detail, a 35×35 -cell *SP-EMS* located at $h = 10$ [m] over the street floor [Fig. 12(a)] has been designed to cover either the irregular region \mathcal{A}_1 [Fig. 12(b)] or both regions \mathcal{A}_1 and \mathcal{A}_2 [Fig. 12(b)].

Once again, there is a non-negligible pros in using the *EMS* synthesis based on the *NS* currents as pointed out by the maps of the local power improvement index $\mathcal{P}_{\mathcal{D}^{opt}\mathcal{D}^{PI}}(\mathbf{r})$ ($\mathbf{r} \in \Theta$) in Fig. 13(b) and Fig. 14(b), respectively, where the peak of the power efficiency improvement turns out to be close to $\mathcal{P}_{\max} \approx 20$ % (vs. $\mathcal{P}_{\max} \approx 28$ % for the pencil beam case) in both test cases despite the complex coverage requirements. For completeness, the color level plots of the reflected field $\mathbf{E}^{refl}(\mathbf{r}|\mathcal{D}^{opt})$ ($\mathbf{r} \in \Theta$) are reported in Fig. 13(a) and Fig. 14(a), as well.

4.2 Experimental Assessment

In order to experimentally assess the reliability of the proposed *EMS* synthesis method, a small-scale cardboard-printed *SP-EMS* prototype has been manufactured and measured (Fig. 15). More in detail, the optimized $P \times Q = 15 \times 15$ design evaluated in Fig. 10(b) has been

fabricated by depositing a conductive ink on a standard cardboard with thickness 2.08×10^{-3} [m]. To comply with the printing area of the available Voltera V-One printer [Fig. 15(a)], the monolithic *EMS* panel has been subdivided in 5×3 parts then assembled by adding an adhesive copper sheet as the ground-plane. Successively, the overall arrangement has been mounted on a wooden panel to guarantee the rigidity of the structure when undergoing the experimental measurement phase [Fig. 15(b)].

As shown in Fig. 15, the agreement between measured and simulated values of the normalized field pattern, reflected by the *SP-EMS* when illuminated by a linearly polarized *TE* field, is very satisfactory.

5 Conclusions

An innovative technique for the improvement of the performance of inexpensive *SP-EMS*s has been presented. By leveraging on the non-uniqueness of the *IS* problem associated to the *SP-EMS* design, the surface current induced on the *EMS* aperture has been decomposed into *PI* and *NS* components. Successively, the unknown *EMS* layout and *NS* expansion coefficients have been determined through an alternate minimization of the mismatch between the ideal surface current, which radiates the user-defined target field, and that induced on the *EMS* layout. Results from a representative set of numerical experiments, concerned with the design of *EMS*s reflecting pencil-beam as well as contoured target patterns, have been reported to assess the feasibility and the effectiveness of the proposed method in improving the performance of inexpensive *EMS* realizations. The measurements on an *EMS* prototype, featuring a conductive ink pattern printed on a standard paper substrate, have been also shown to prove the reliability of the synthesis process.

From the numerical validation and performance assessment, the following main outcomes can be drawn: (a) the proposed *SP-EMS* synthesis method enables a non-negligible improvement, in terms of reflected power control, over traditional (i.e., *PI*-based) design approaches when adopting inexpensive *EMS* meta-atoms; (b) the performance improvement is more significant for smaller *EMS* apertures, thus one can infer that it is more efficient to implement a *SP-EMS* by assembling small modular tiles instead of realizing a wide monolithic support; (c) the *NS*-based

synthesis is competitive in dealing with simple (e.g., pencil beam) as well as complex (e.g., shaped beam) footprint requirements, while the performance (within a quite large range) are almost independent on the reflection angle $(\theta^{refl}, \varphi^{refl})$; (d) the proposed method is reliable since it carefully predicts the performance of *EMS* prototypes (Fig. 15).

Future works, beyond the scope of this manuscript, will be aimed at extending the previous design strategy to dynamically-adaptive architectures such as *RIS*s. Thanks to the generality of the proposed approach, the possibility to include further design constraints is under investigation.

Acknowledgements

This work benefited from the networking activities carried out within the project DICAM-EXC (Departments of Excellence 2023-2027, grant L232/2016) funded by the Italian Ministry of Education, Universities and Research (MUR), the Project "Smart ElectroMagnetic Environment in TrentiNo - SEME@TN" funded by the Autonomous Province of Trento (CUP: C63C22000720003), the Project "AURORA - Smart Materials for Ubiquitous Energy Harvesting, Storage, and Delivery in Next Generation Sustainable Environments" funded by the Italian Ministry for Universities and Research within the PRIN-PNRR 2022 Program, and the following projects funded by the European Union - NextGenerationEU within the PNRR Program: Project "ICSC National Centre for HPC, Big Data and Quantum Computing (CN HPC)" (CUP: E63C22000970007), Project "Telecommunications of the Future (PE00000001 - program "RESTART", Structural Project 6GWINET)" (CUP: D43C22003080001), Project "INSIDE-NEXT - Indoor Smart Illuminator for Device Energization and Next-Generation Communications" (CUP: E53D23000990001), and Project "Telecommunications of the Future (PE00000001 - program "RESTART", Focused Project MOSS)" (CUP: J33C22002880001). A. Massa wishes to thank E. Vico for her never-ending inspiration, support, guidance, and help.

References

- [1] A. Massa, A. Benoni, P. Da Ru, S. K. Goudos, B. Li, G. Oliveri, A. Polo, P. Rocca, and M. Salucci, "Designing smart electromagnetic environments for next-generation wireless

- communications,” *Telecom*, vol. 2, no. 2, pp. 213-221, 2021.
- [2] F. Yang, D. Erricolo, and A. Massa, “Guest Editorial - Smart Electromagnetic Environment,” *IEEE Trans. Antennas Propag.*, vol. 70, no. 10, pp. 8687-8690, Oct. 2022.
- [3] M. Barbuto, Z. Hamzavi-Zarghani, M. Longhi, A. Monti, D. Ramaccia, S. Vellucci, A. Toscano, and F. Bilotti, “Metasurfaces 3.0: a new paradigm for enabling smart electromagnetic environments,” *IEEE Trans. Antennas Propag.*, vol. 70, no. 10, pp. 8883-8897, Oct. 2022.
- [4] M. Di Renzo, M. Debbah, D.-T. Phan-Huy, A. Zappone, M.-S. Alouini, C. Yuen, V. Sciancalepore, G. C. Alexandropoulos, J. Hoydis, H. Gacanin, J. De Rosny, A. Bounceur, G. Lerosey, and M. Fink, “Smart radio environments empowered by reconfigurable AI metasurfaces: An idea whose time has come,” *EURASIP J. Wireless Commun. Netw.*, vol. 129, pp. 1-20, 2019.
- [5] M. Di Renzo, A. Zappone, M. Debbah, M.-S. Alouini, C. Yuen, J. De Rosny, and S. Tretyakov, “Smart radio environments empowered by reconfigurable intelligent surfaces: How it works, state of research, and the road ahead,” *IEEE J. Sel. Areas Comm.*, vol. 38, no. 11, pp. 2450-2525, Nov. 2020.
- [6] M. Di Renzo, K. Ntontin, J. Song, F. H. Danufane, X. Qian, F. Lazarakis, J. De Rosny, D.-T. Phan-Huy, O. Simeone, R. Zhang, M. Debbah, G. Lerosey, M. Fink, S. Tretyakov, and S. Shamai, “Reconfigurable intelligent surfaces vs. relaying: Differences, similarities, and performance comparison,” *IEEE Open J. Comm. Soc.*, vol. 1, pp. 798-807, 2020.
- [7] C. Huang, A. Zappone, G. C. Alexandropoulos, M. Debbah, and C. Yuen, “Reconfigurable intelligent surfaces for energy efficiency in wireless communication,” *IEEE Trans. Wireless Commun.*, vol. 18, no. 8, pp. 4157-4170, Aug. 2019.
- [8] G. Oliveri, P. Rocca, M. Salucci, and A. Massa, “Holographic smart EM skins for advanced beam power shaping in next generation wireless environments,” *IEEE J. Multiscale Multiphysics Computat. Techn.*, vol. 6, pp. 171-182, Oct. 2021.

- [9] G. Oliveri, F. Zardi, P. Rocca, M. Salucci, and A. Massa, "Building a smart EM environment - AI-Enhanced aperiodic micro-scale design of passive EM skins," *IEEE Trans. Antennas Propag.*, vol. 70, no. 10, pp. 8757-8770, Oct. 2022.
- [10] G. Oliveri, F. Zardi, P. Rocca, M. Salucci and A. Massa, "Constrained design of passive static EM skins," *IEEE Trans. Antennas Propag.*, vol. 71, no. 2, pp. 1528-1538, Feb. 2023.
- [11] G. Oliveri, M. Salucci, and A. Massa, "Generalized Analysis and Unified Design of EM Skins," *IEEE Trans. Antennas Propag.*, vol. 71, no.8, pp. 6579-6592, Aug.2023.
- [12] A. F. Vaquero, E. Martinez-de-Rioja, M. Arrebola, J. A. Encinar and M. Achour, "Smart electromagnetic skin to enhance near-field coverage in mm-Wave 5G indoor scenarios," *IEEE Trans. Antennas Propag.*, vol. 72, no. 5, pp. 4311-4326, May 2024.
- [13] F. Yang and Y. Rahmat-Samii, *Surface Electromagnetics with Applications in Antenna, Microwave, and Optical Engineering*, Cambridge, UK: Cambridge University Press, 2019.
- [14] A. Alu, N. Engheta, A. Massa, and G. Oliveri, Eds., *Metamaterials-by-Design: Theory, Technologies, and Vision*. Amsterdam, NL: Elsevier, 2024.
- [15] P. Rocca, M. Benedetti, M. Donelli, D. Franceschini, and A. Massa, "Evolutionary optimization as applied to inverse problems," *Inv. Probl.*, vol. 25, art no. 123003, pp. 1-41, Dec. 2009.
- [16] L. Yang, A. Rida, R. Vyas, and M. M. Tentzeris, "RFID tag and RF structures on a paper substrate using inkjet-printing technology," *IEEE Trans. Microw. Theory Techn.*, vol. 55, no. 12, pp. 2894-2901, Dec. 2007.
- [17] I. V. Lindell and A. Sihvola, *Boundary Conditions in Electromagnetics*. IEEE Press, 2019.
- [18] A. Osipov and S. Tretyakov, *Modern electromagnetic scattering theory with applications*. John Wiley & Sons, 2017.

- [19] M. Salucci, L. Tenuti, G. Oliveri, and A. Massa, "Efficient prediction of the EM response of reflectarray antenna elements by an advanced statistical learning method," *IEEE Trans. Antennas Propag.*, vol. 66, no. 8, pp. 3995-4007, Aug. 2018.
- [20] G. Oliveri, M. Salucci, and A. Massa, "Towards efficient reflectarray digital twins - An EM-driven machine learning perspective," *IEEE Trans. Antennas Propag.*, vol. 70, no. 7, pp. 5078-5093, Jul. 2022.
- [21] ANSYS Electromagnetics Suite - HFSS (2021). ANSYS, Inc.
- [22] M. Bertero and P. Boccacci, *Introduction to Inverse Problems in Imaging*, U.K., Bristol: IoP Publishing, 1998.
- [23] P. M. van den Berg and A. Abubakar, "Inverse scattering algorithms based on contrast source integral representations," *Inverse Probl. Eng.*, vol. 10, no. 6, pp. 559-576, 2002.
- [24] Y. Kawahara, S. Hodges, N.-W. Gong, S. Olberding, and J. Steimle, "Building functional prototypes using conductive inkjet printing," *IEEE Pervasive Comput.*, vol. 13, no. 3, pp. 30-38, Jul. 2014.
- [25] F. Alimenti, P. Mezzanotte, M. Dionigi, M. Virili, and L. Roselli, "Microwave circuits in paper substrates exploiting conductive adhesive tapes," *IEEE Microw. Wireless Compon. Lett.*, vol. 22, no. 12, pp. 660-662, Dec. 2012.
- [26] M. Borgese, F. A. Dicandia, F. Costa, S. Genovesi, and G. Manara, "An inkjet printed chipless RFID sensor for wireless humidity monitoring," *IEEE Sensors J.*, vol. 17, no. 15, pp. 4699-4707, Aug. 2017.
- [27] S. Genovesi, F. Costa, F. Fanciulli, and A. Monorchio, "Wearable inkjet-printed wideband antenna by using miniaturized AMC for sub-GHz applications," *IEEE Antennas Wireless Propag. Lett.*, vol. 15, pp. 1927-1930, Jan. 2016.
- [28] H. Legay, D. Bresciani, E. Labiole, R. Chiniard, and R. Gillard, "A multi facets composite panel reflectarray antenna for a space contoured beam antenna in Ku band," *PIER B*, vol. 54, pp. 1-26, 2013.

- [29] P. Rocca, P. Da Ru, N. Anselmi, M. Salucci, G. Oliveri, D. Erricolo, and A. Massa, “On the design of modular reflecting EM skins for enhanced urban wireless coverage,” *IEEE Trans. Antennas Propag.*, vol. 70, no. 10, pp. 8771-8784, Oct. 2022.

FIGURE CAPTIONS

- **Figure 1.** *Mathematical Formulation* - Sketch of the *SP-EMS* design problem.
- **Figure 2.** *Illustrative Example* - Sketch of the meta-atom geometry (a) and plots of (b) the magnitude and (c) the phase of $\Gamma_{TE}(d^{(1)})$ vs. $d^{(1)}$.
- **Figure 3.** *Illustrative Example* ($h = 5$ [m], $P \times Q = 35 \times 35$) - Plots of (a) $\left| \tilde{\mathbf{E}}^{refl}(\mathbf{r}) \right|$ ($\mathbf{r} \in \Theta$) and (b) the normalized \mathcal{L} spectrum $\{\hat{\sigma}_s; s = 1, \dots, S\}$.
- **Figure 4.** *Illustrative Example* ($h = 5$ [m], $P \times Q = 35 \times 35$, $(\theta^{refl}, \varphi^{refl}) = (30, -45)$ [deg], paper substrate) - Plots of (a) $\underline{\beta}^{opt}$ and (b) the *SP-EMS* \mathcal{D}^{opt} layout.
- **Figure 5.** *Illustrative Example* ($h = 5$ [m], $P \times Q = 35 \times 35$, $(\theta^{refl}, \varphi^{refl}) = (30, -45)$ [deg], paper substrate) - Plots of (a) $\left| \mathbf{E}^{refl}(\mathbf{r}|\mathcal{D}^{opt}) \right|$, (b) $\left| \mathbf{E}_{PI}^{refl}(\mathbf{r}) \right|$, (c) $\left| \mathbf{E}_{NS}^{refl}(\mathbf{r}) \right|$, and (d) $\left| \mathbf{E}_{TOT}^{refl}(\mathbf{r}) \right|$ ($\mathbf{r} \in \Theta$).
- **Figure 6.** *Illustrative Example* ($h = 5$ [m], $P \times Q = 35 \times 35$, $(\theta^{refl}, \varphi^{refl}) = (30, -45)$ [deg], electric $\hat{\mathbf{y}}$ component) - Plots of (a)(c)(e) the magnitude and (b)(d)(f) the phase of (a)(b) $\mathbf{J}_{PI}(\mathbf{r})$, (c)(d) $\mathbf{J}_{NS}(\mathbf{r}|\underline{\beta})$, and (e)(f) $\tilde{\mathbf{J}}(\mathbf{r}|\underline{\beta})$ ($\mathbf{r} \in \Omega$).
- **Figure 7.** *Illustrative Example* ($h = 5$ [m], $P \times Q = 35 \times 35$, $(\theta^{refl}, \varphi^{refl}) = (30, -45)$ [deg], paper substrate) - Pictures of (a) the *SP-EMS* \mathcal{D}^{PI} layout (a) and maps of the corresponding (b) $\left| \mathbf{E}^{refl}(\mathbf{r}|\mathcal{D}^{PI}) \right|$ and (c) $\mathcal{P}_{\mathcal{D}^{opt}\mathcal{D}^{PI}}(\mathbf{r})$ distributions ($\mathbf{r} \in \Theta$).
- **Figure 8.** *Illustrative Example* ($h = 5$ [m], $P \times Q = 35 \times 35$, $(\theta^{refl}, \varphi^{refl}) = (30, -45)$ [deg], ISOLA substrate) - Pictures of (a) the *SP-EMS* \mathcal{D}_{ISOLA}^{PI} layout and map of the corresponding (b) $\left| \mathbf{E}^{refl}(\mathbf{r}|\mathcal{D}^{PI}) \right|$ distribution ($\mathbf{r} \in \Theta$).

- **Figure 9.** *Illustrative Example* ($h = 5$ [m], $P \times Q = 35 \times 35$, $(\theta^{refl}, \varphi^{refl}) = (30, -45)$ [deg]) - Plots of (a) $|\mathbf{E}^{refl}(\mathbf{r}|\mathcal{D})|$ in the $\varphi = \varphi^{refl}$ -cut and maps of (b) $\mathcal{P}_{\mathcal{D}_{paper}^{PI} \mathcal{D}_{ISOLA}^{PI}}(\mathbf{r})$ and (c) $\mathcal{P}_{\mathcal{D}_{paper}^{opt} \mathcal{D}_{isola}^{PI}}(\mathbf{r})$ distributions ($\mathbf{r} \in \Theta$).
- **Figure 10.** *Numerical Results* ($h = 5$ [m], $(\theta^{refl}, \varphi^{refl}) = (30, -45)$ [deg]) - Plots of (a) \mathcal{P}_{\max} versus P ($= Q$) and (b) $|\mathbf{E}^{refl}(\mathbf{r}|\mathcal{D})|$ in the $\varphi = \varphi^{refl}$ -cut when $P \times Q = \{15 \times 15, 95 \times 95\}$.
- **Figure 11.** *Numerical Results* ($h = 5$ [m], $P \times Q = 35 \times 35$, $\varphi^{refl} = -45$ [deg]) - Plots of \mathcal{P}_{\max} versus the reflection angle θ^{refl} .
- **Figure 12.** *Numerical Results* ($h = 10$ [m], $P \times Q = 35 \times 35$; Gare du Nord - Paris) - Visualization of (a) the 3D view and (b) the aerial perspective of the *EM* scenario.
- **Figure 13.** *Numerical Results* ($h = 10$ [m], $P \times Q = 35 \times 35$; Gare du Nord - Paris, \mathcal{A}_1 Coverage) - Maps of (a) $|\mathbf{E}^{refl}(\mathbf{r}|\mathcal{D}^{opt})|$ and (b) $\mathcal{P}_{\mathcal{D}^{opt} \mathcal{D}^{PI}}(\mathbf{r})$ ($\mathbf{r} \in \Theta$).
- **Figure 14.** *Numerical Results* ($h = 10$ [m], $P \times Q = 35 \times 35$; Gare du Nord - Paris, $\mathcal{A}_1 \cup \mathcal{A}_2$ Coverage) - Maps of (a) $|\mathbf{E}^{refl}(\mathbf{r}|\mathcal{D}^{opt})|$ and (b) $\mathcal{P}_{\mathcal{D}^{opt} \mathcal{D}^{PI}}(\mathbf{r})$ ($\mathbf{r} \in \Theta$).
- **Figure 15.** *Experimental Results* ($h = 5$ [m], $(\theta^{refl}, \varphi^{refl}) = (30, -45)$ [deg], $P \times Q = 15 \times 15$, $\mathcal{D}_{paper}^{opt}$) - Pictures of (a) the fabrication process, (b) the *SP-EMS* prototype, and (c) the plot of $|\mathbf{E}^{refl}(\mathbf{r}|\mathcal{D})|$ in the $\varphi = \varphi^{refl}$ -cut.

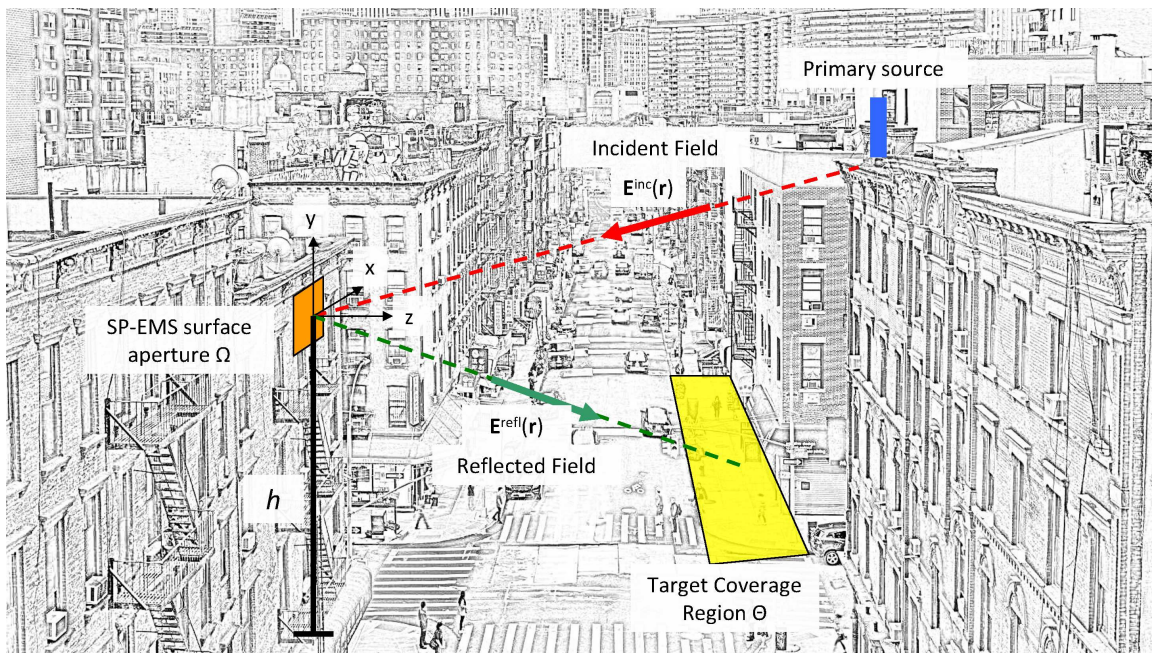
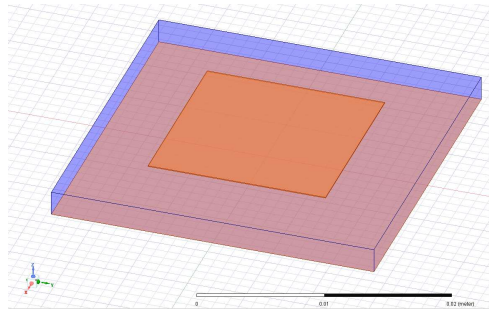
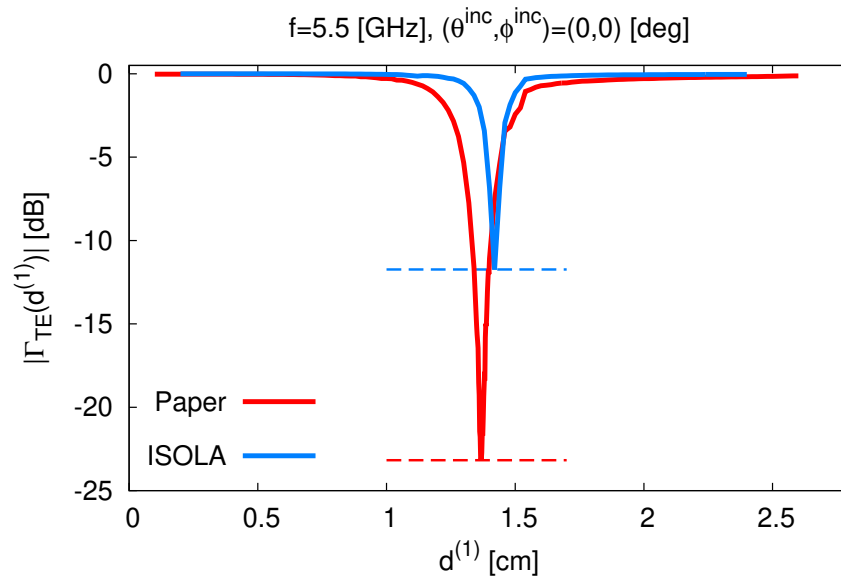


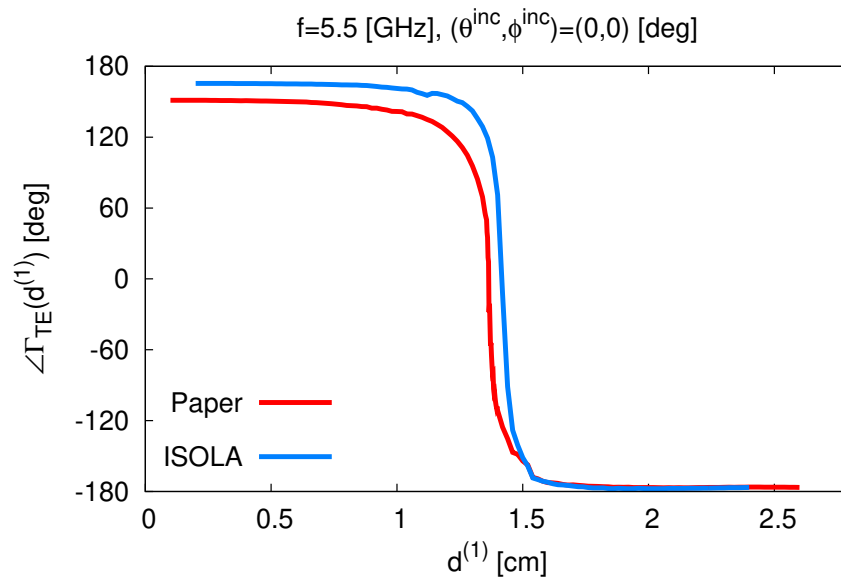
Fig. 1 - G. Oliveri et al., "On the Improvement of the Performance of ..."



(a)



(b)



(c)

Fig. 2 - G. Oliveri et al., “On the Improvement of the Performance of ...”

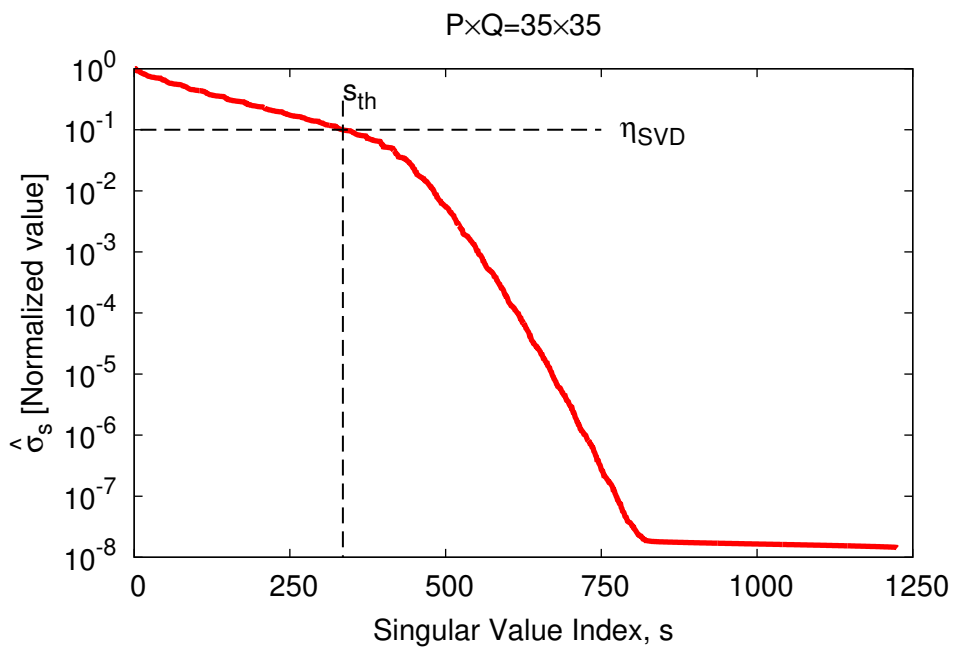
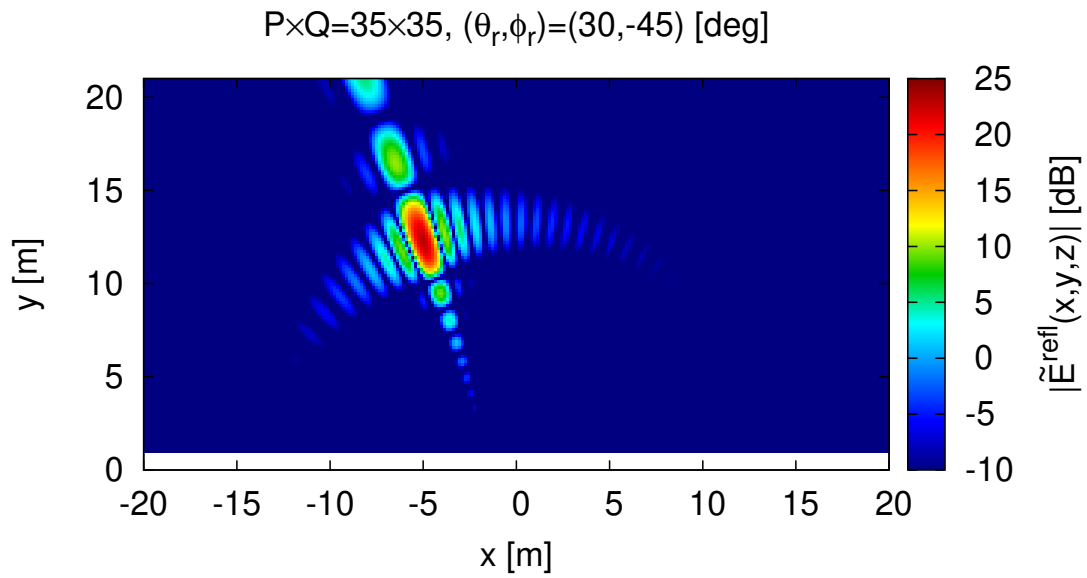


Fig. 3 - G. Oliveri et al., “On the Improvement of the Performance of ...”

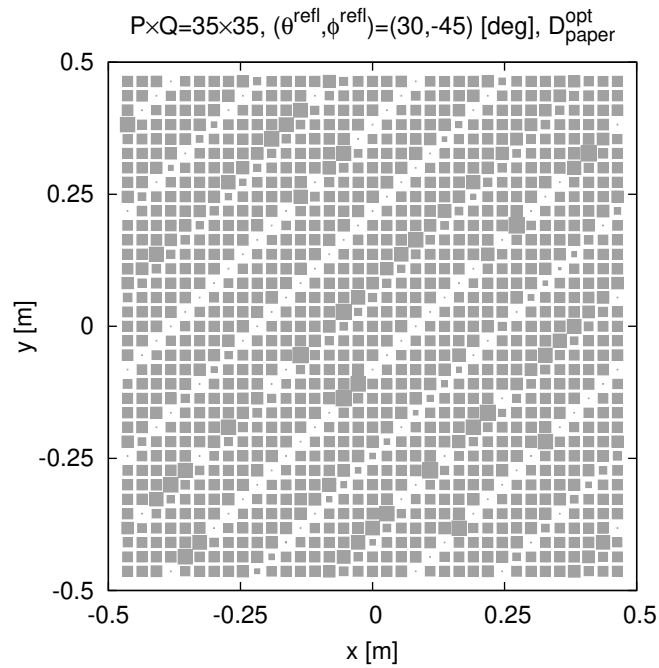
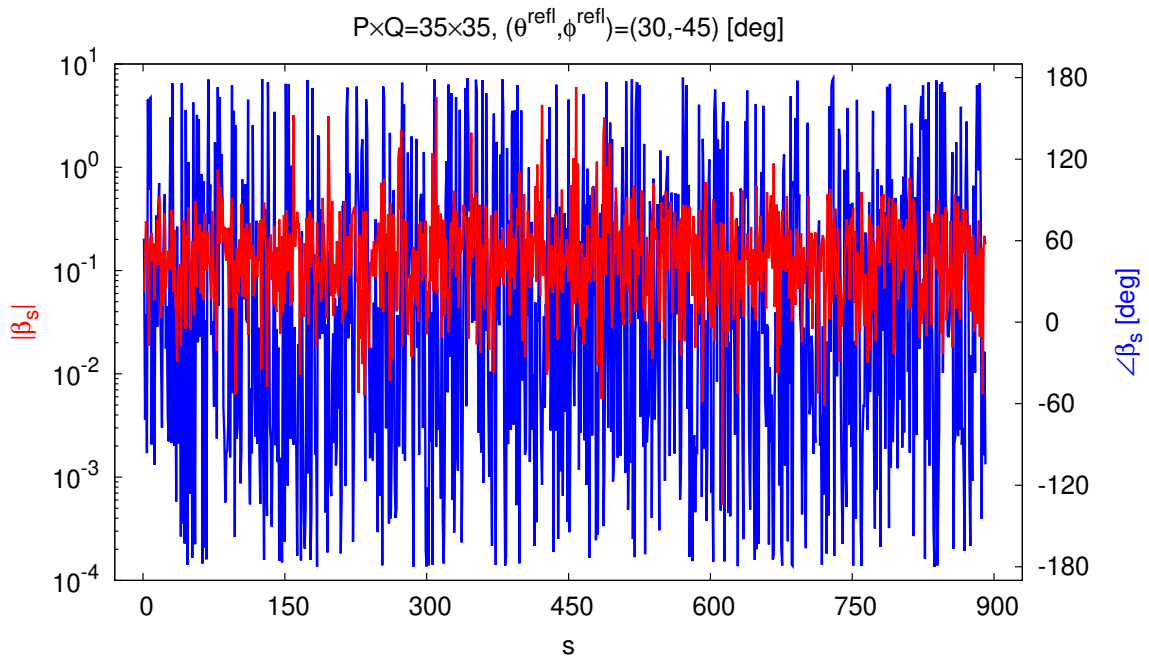
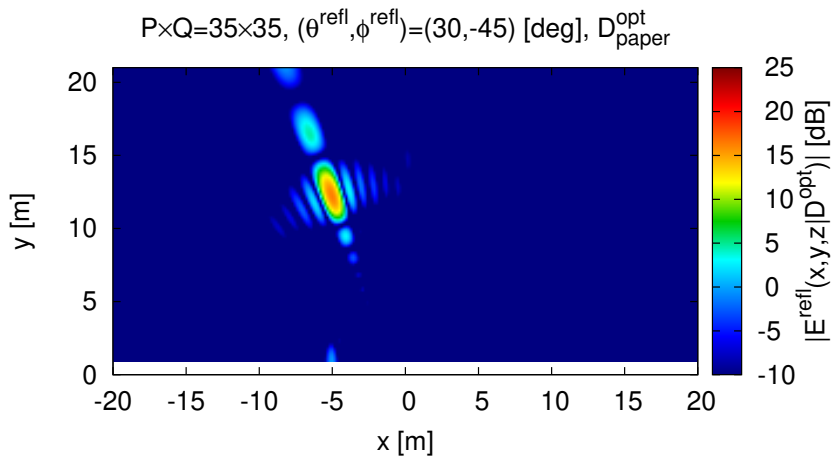
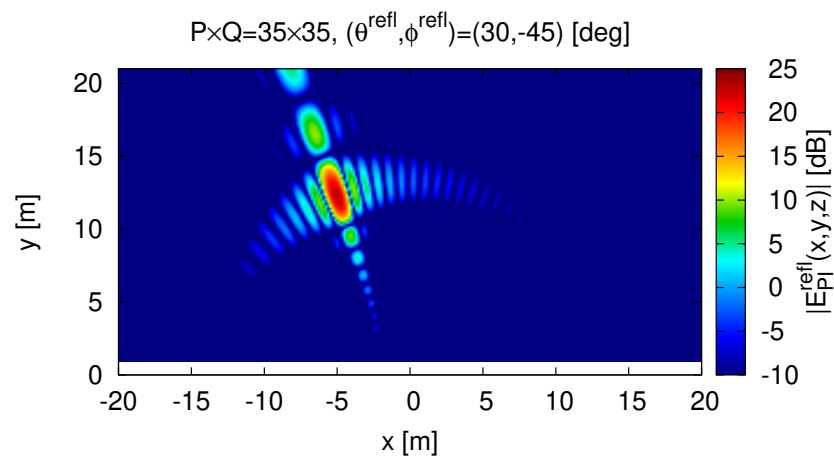


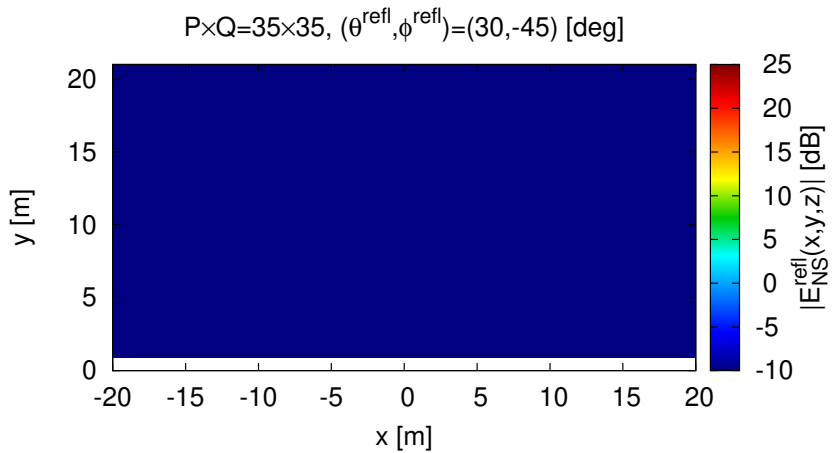
Fig. 4 - G. Oliveri et al., “On the Improvement of the Performance of ...”



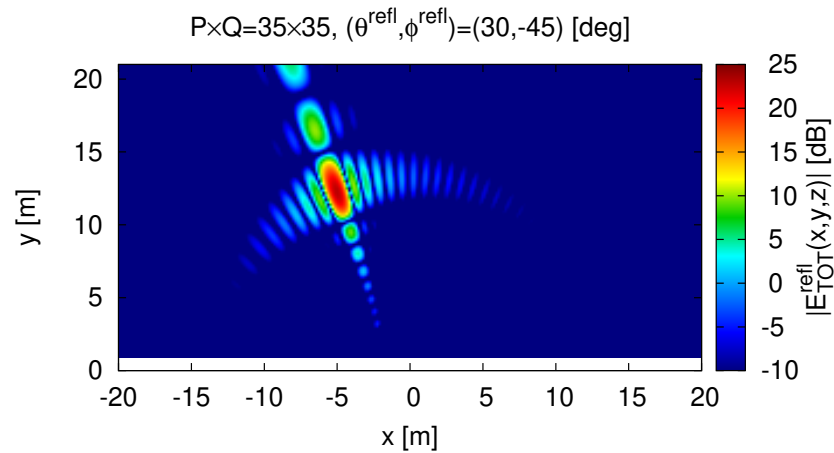
(a)



(b)



(c)



(d)

Fig. 5 - G. Oliveri et al., "On the Improvement of the Performance of ..."

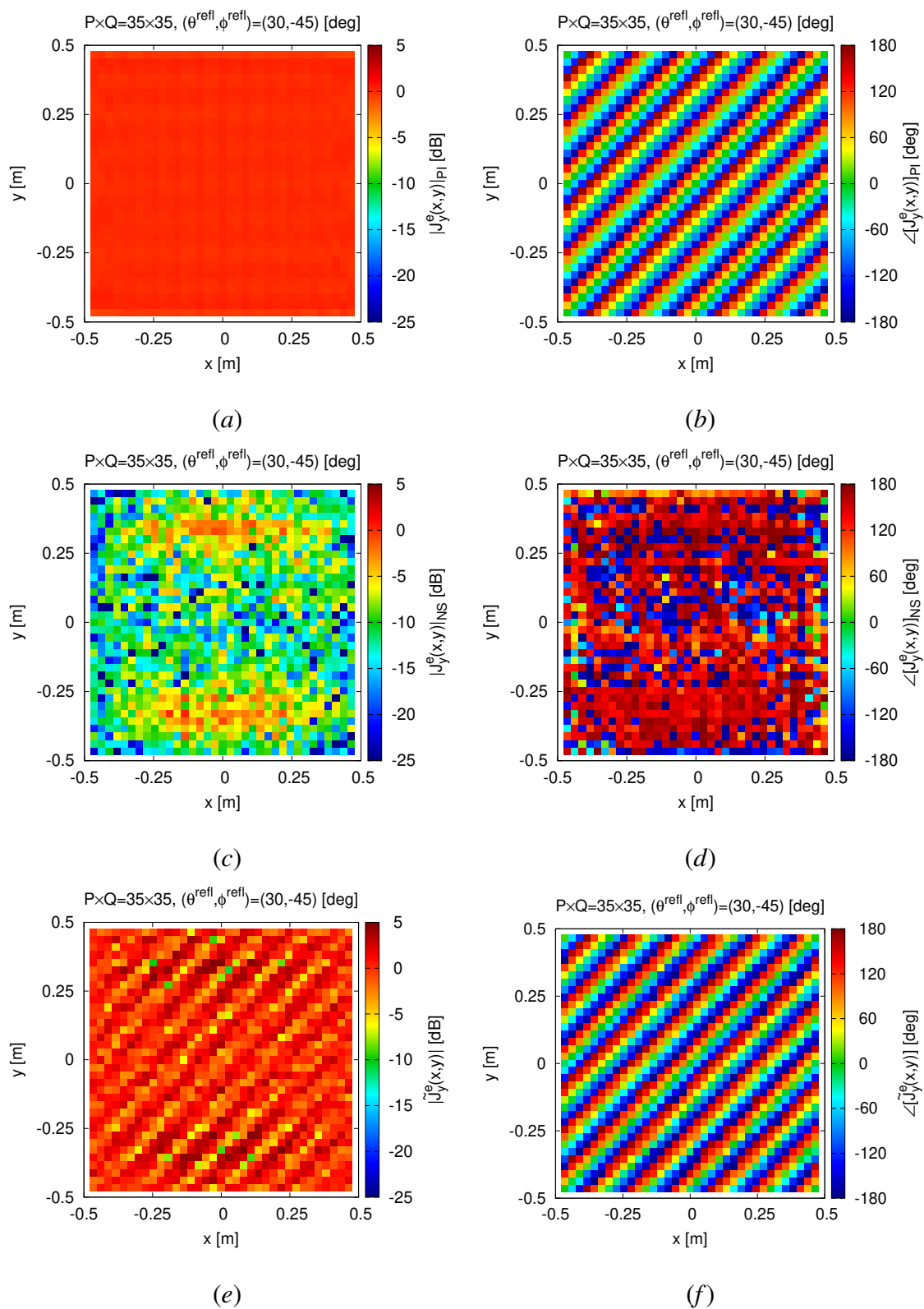


Fig. 6 - G. Oliveri et al., “On the Improvement of the Performance of ...”

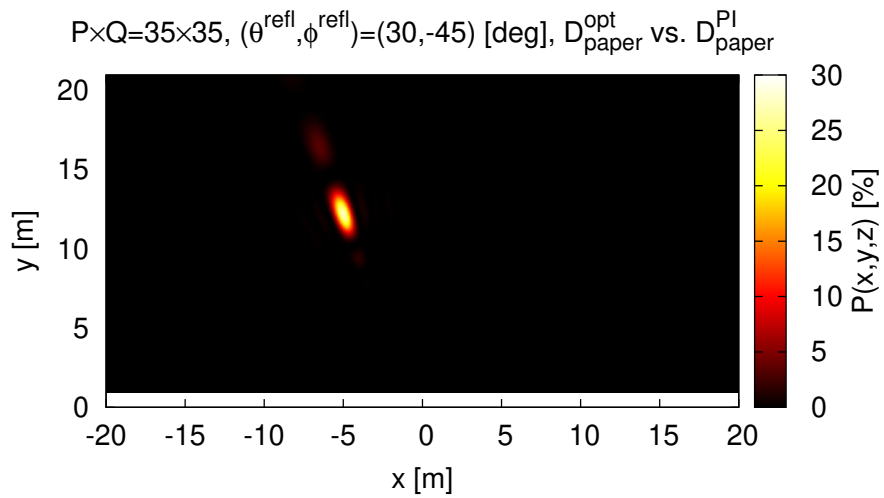
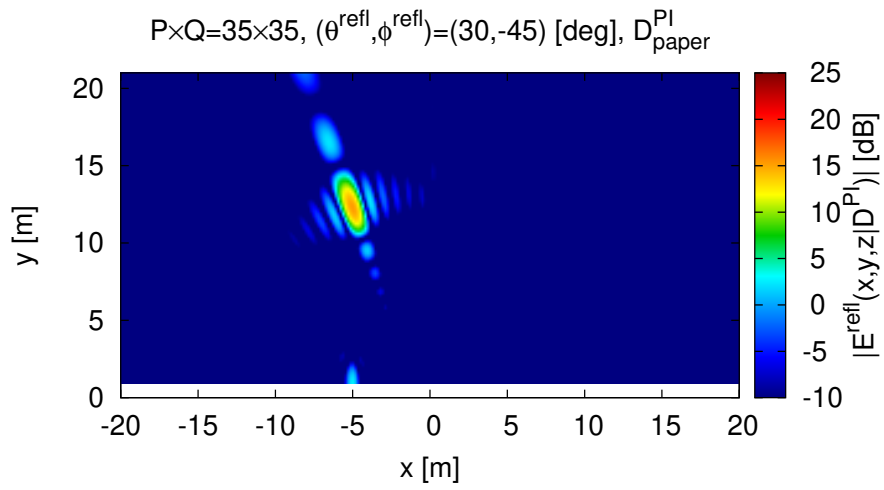
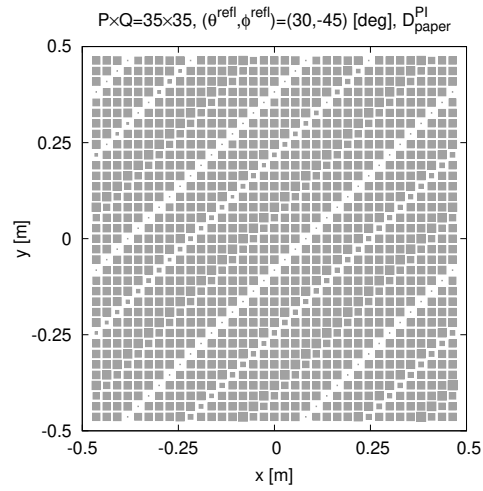
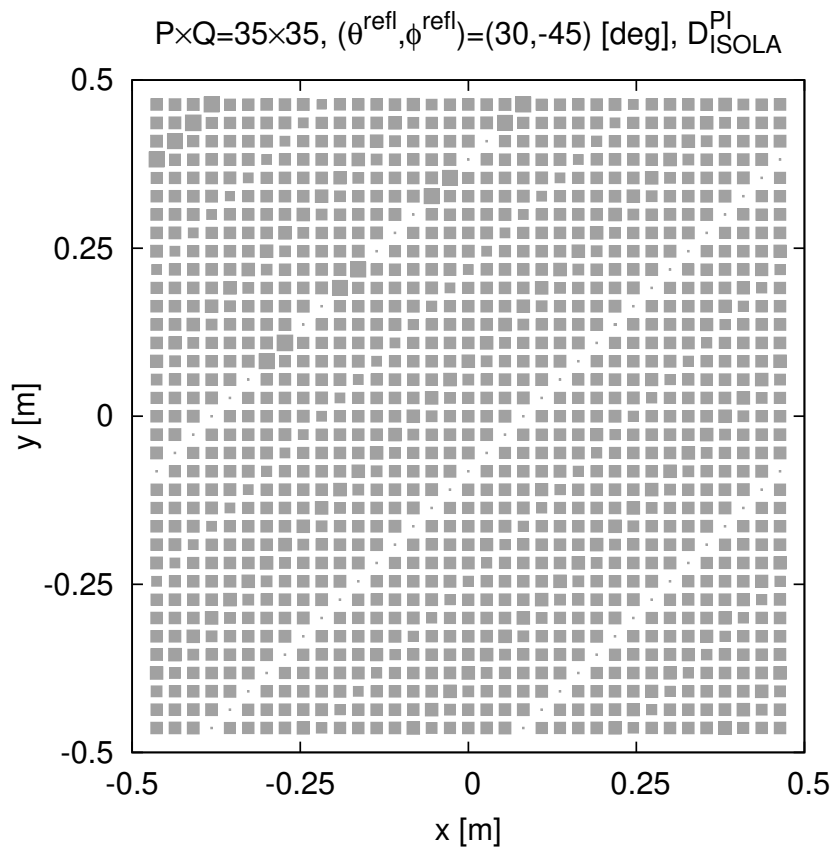
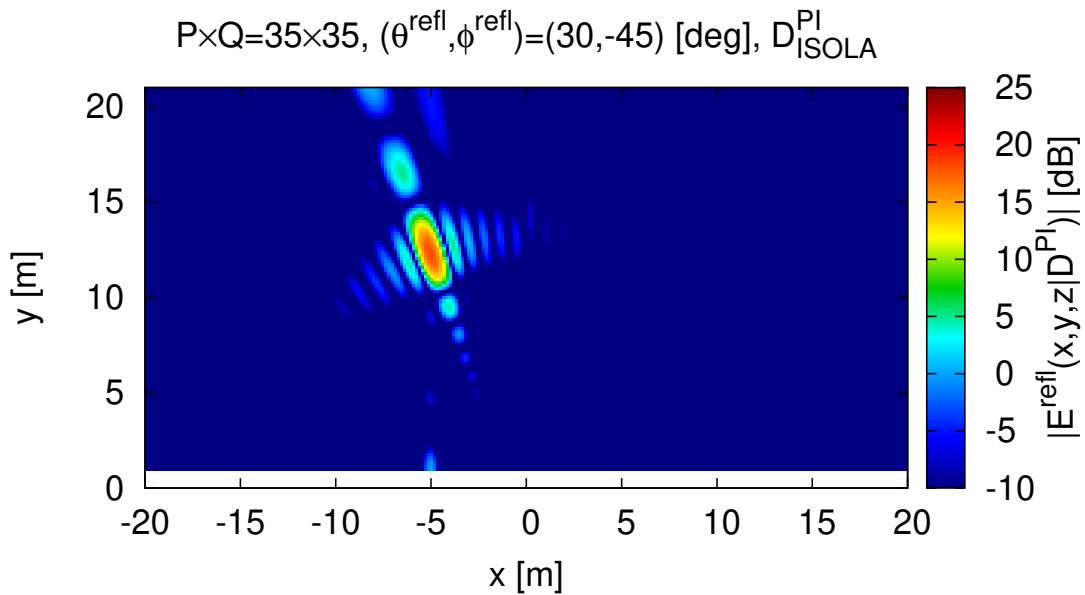


Fig. 7 - G. Oliveri et al., “On the Improvement of the Performance of ...”



(a)



(b)

Fig. 8 - G. Oliveri et al., "On the Improvement of the Performance of ..."

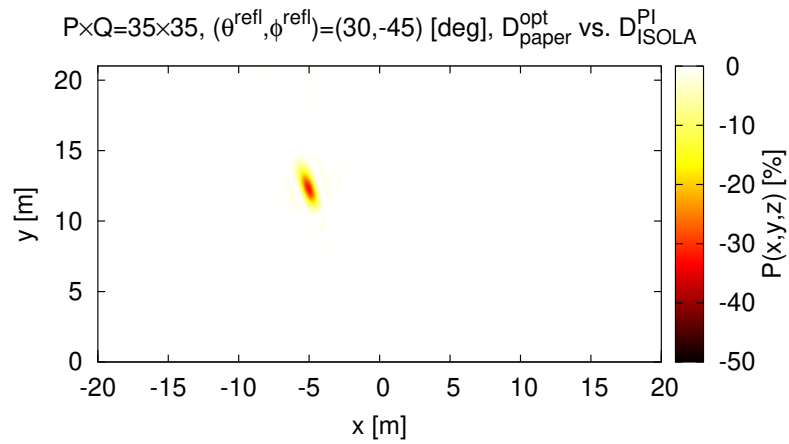
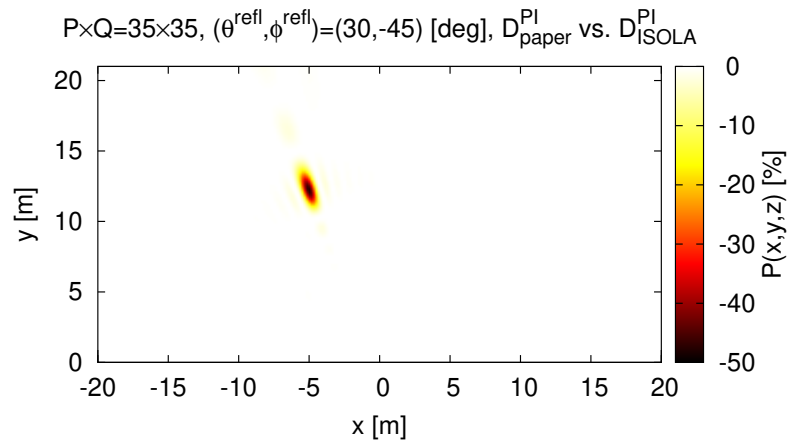
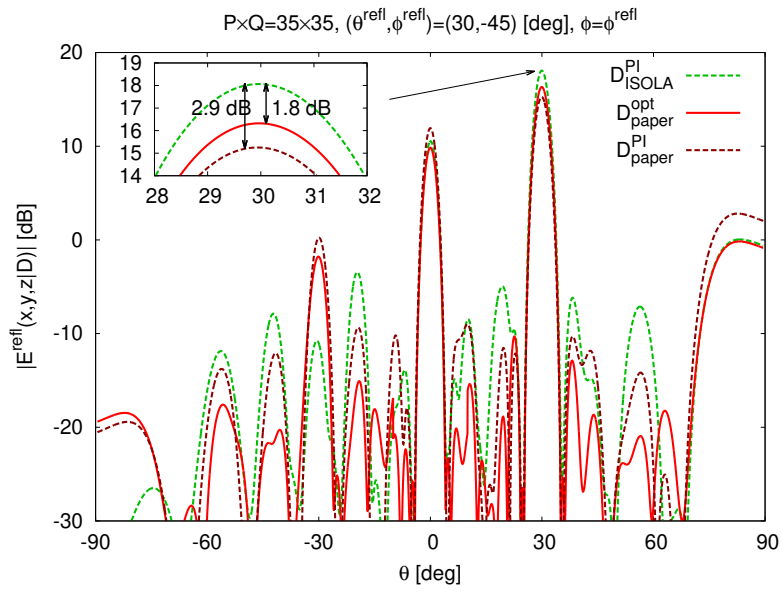
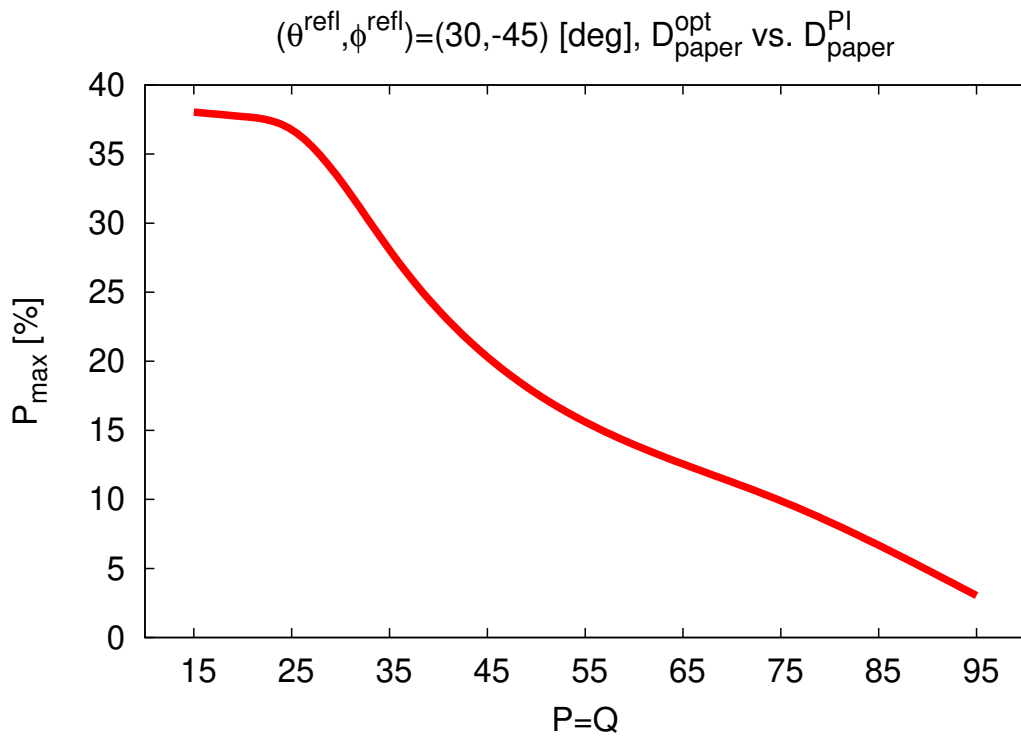
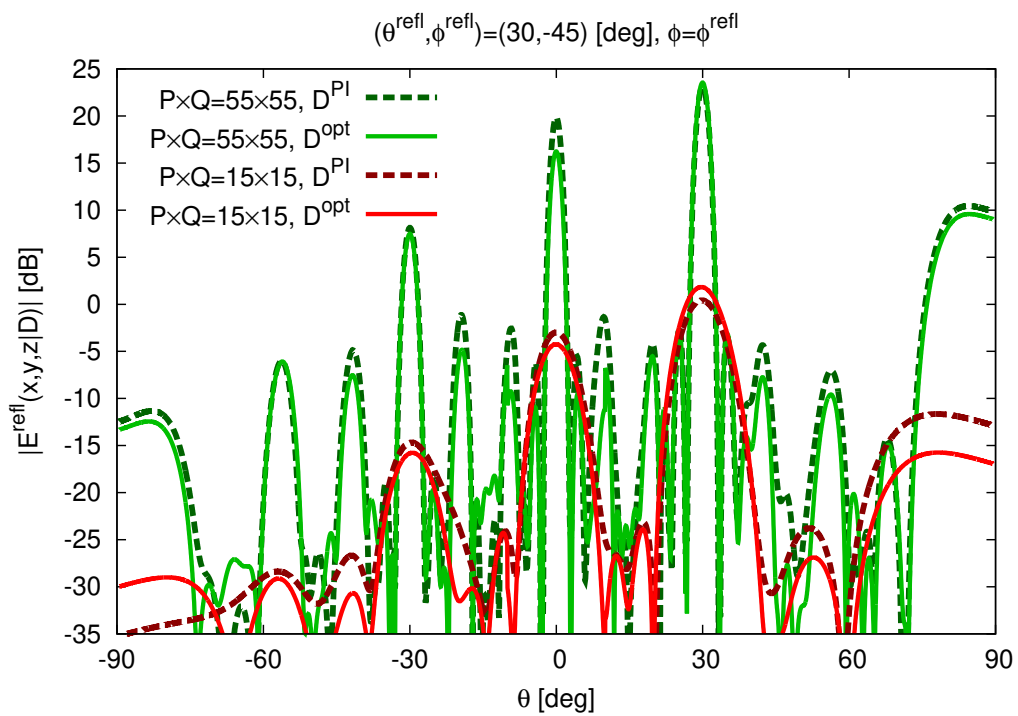


Fig. 9 - G. Oliveri et al., “On the Improvement of the Performance of ...”



(a)



(b)

Fig. 10 - G. Oliveri et al., "On the Improvement of the Performance of ..."

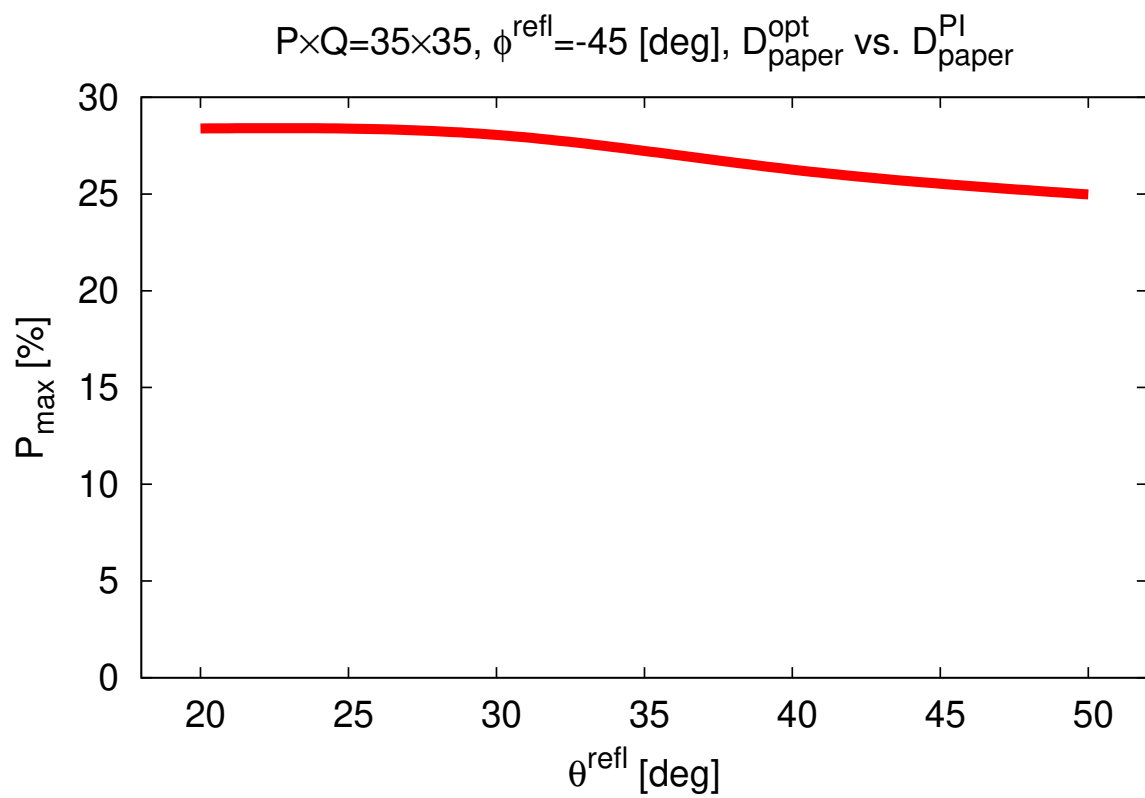
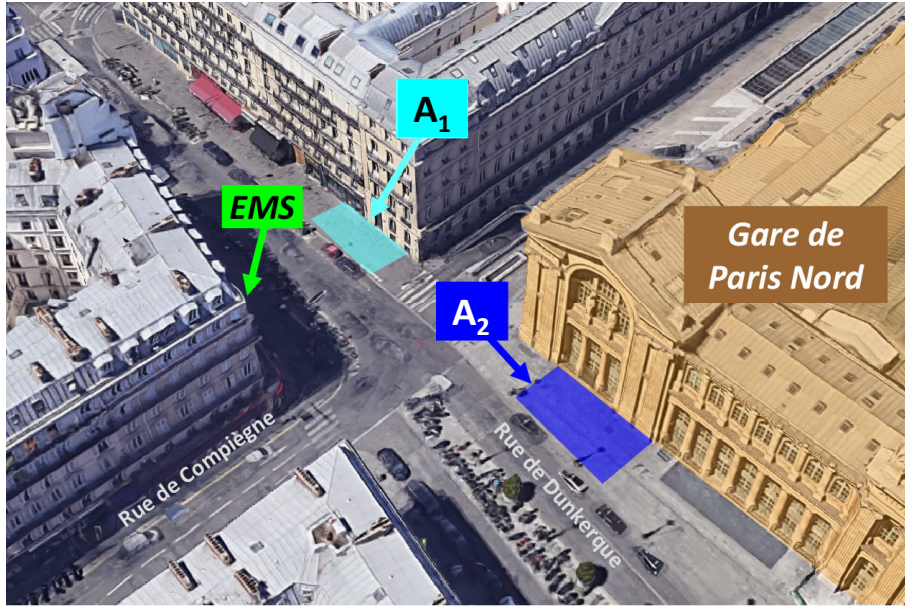
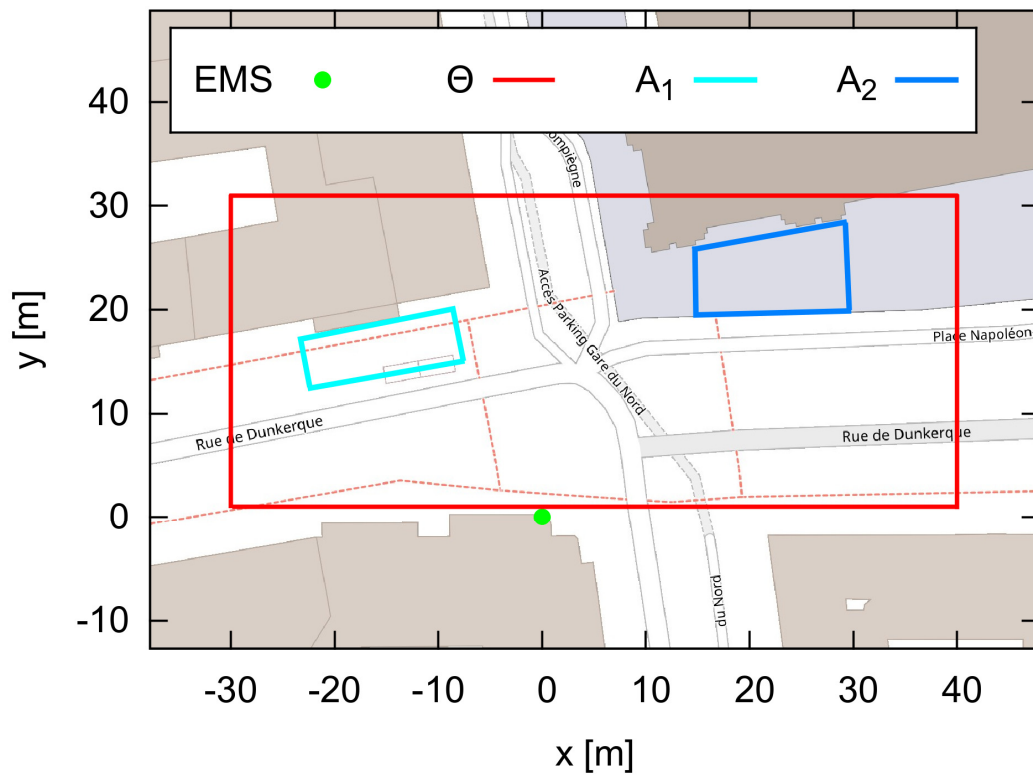


Fig. 11 - G. Oliveri et al., “On the Improvement of the Performance of ...”



(a)



(b)

Fig. 12 - G. Oliveri et al., “On the Improvement of the Performance of ...”

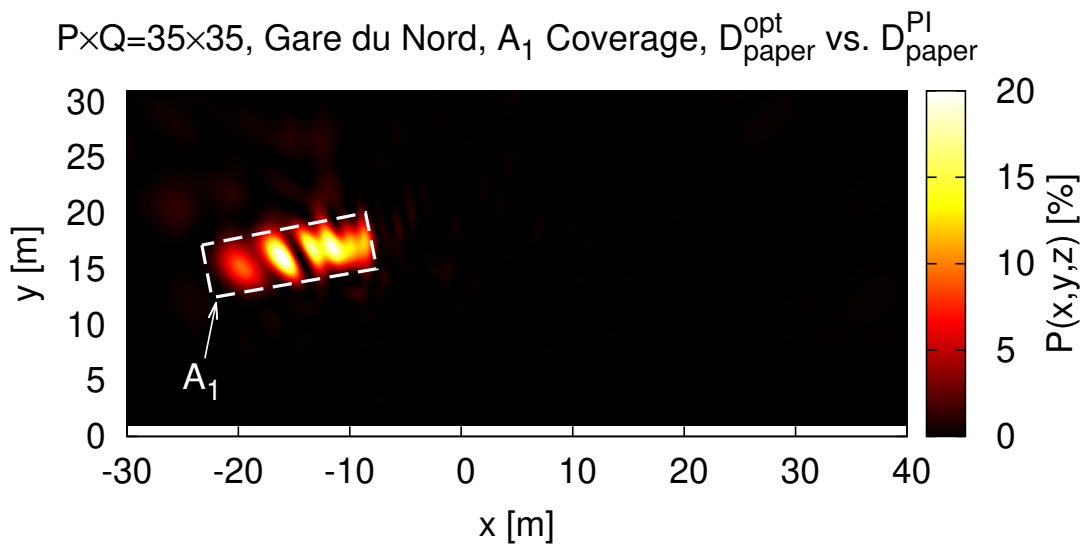
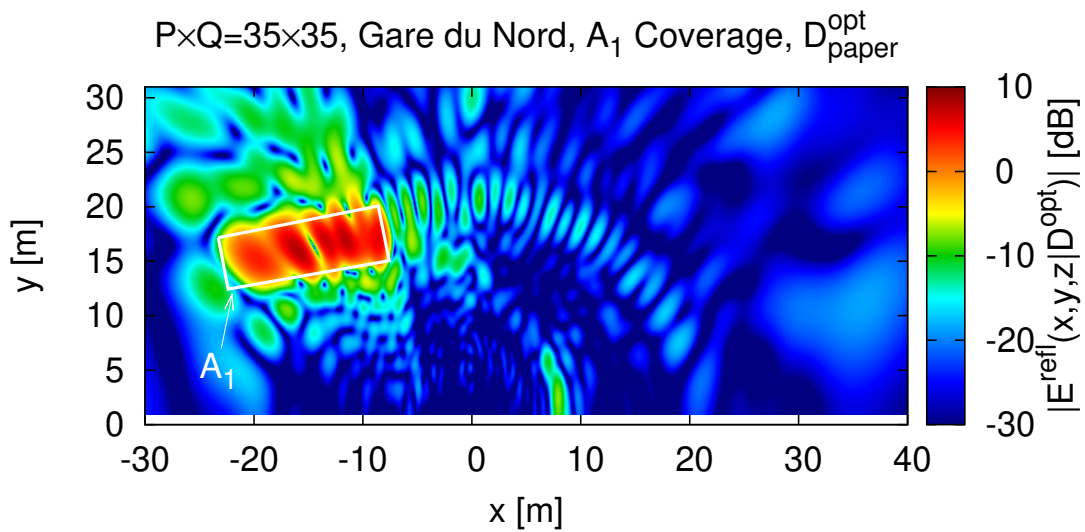
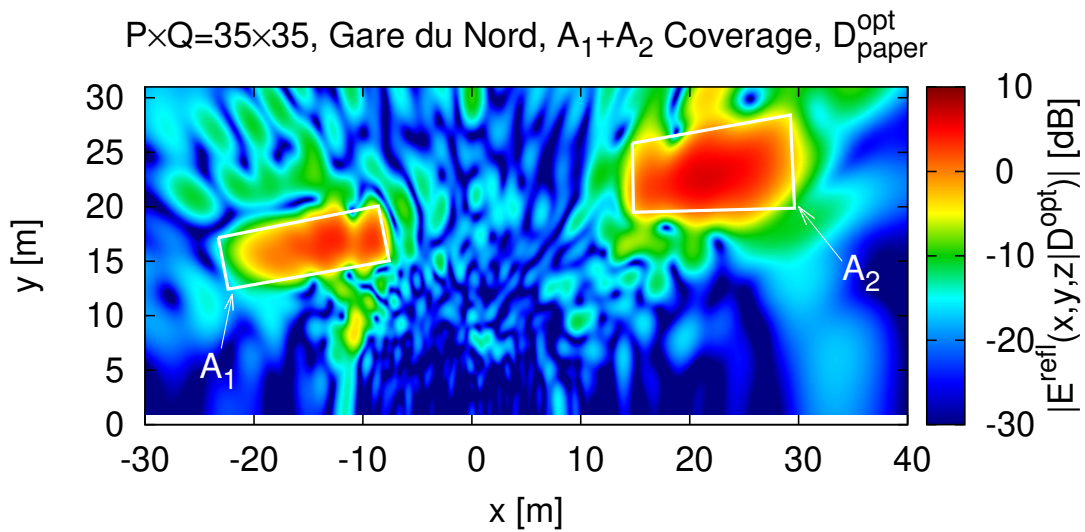
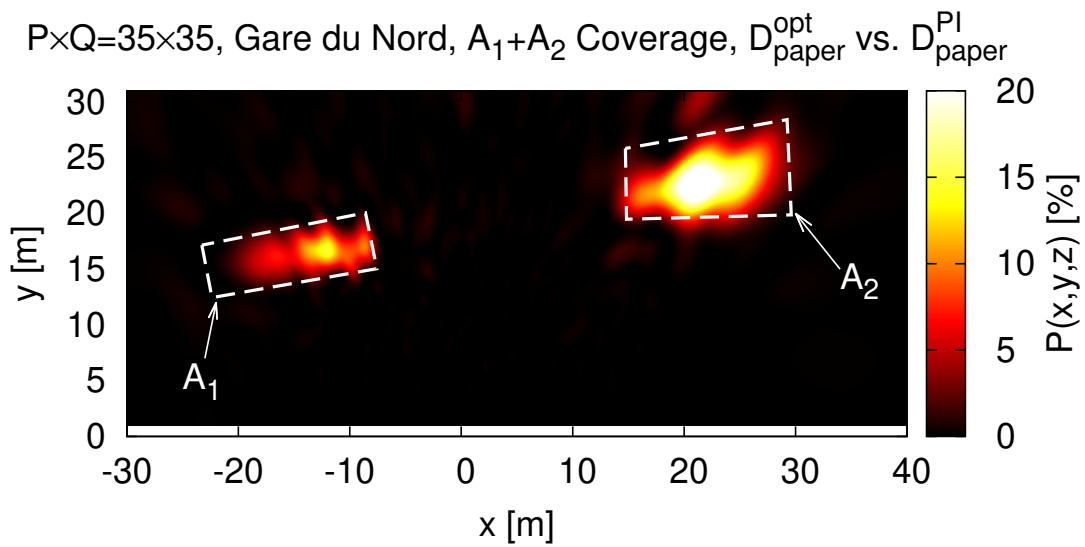


Fig. 13 - G. Oliveri et al., “On the Improvement of the Performance of ...”

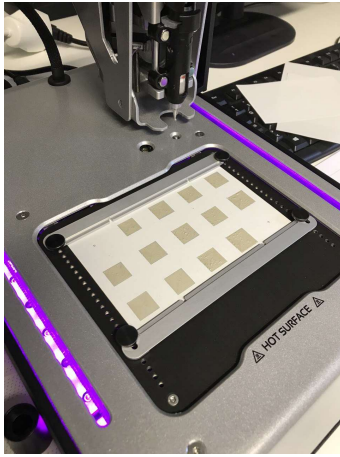


(a)

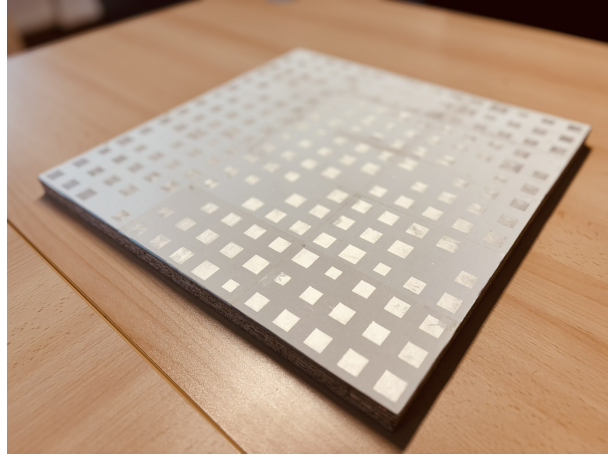


(b)

Fig. 14 - G. Oliveri et al., "On the Improvement of the Performance of ..."

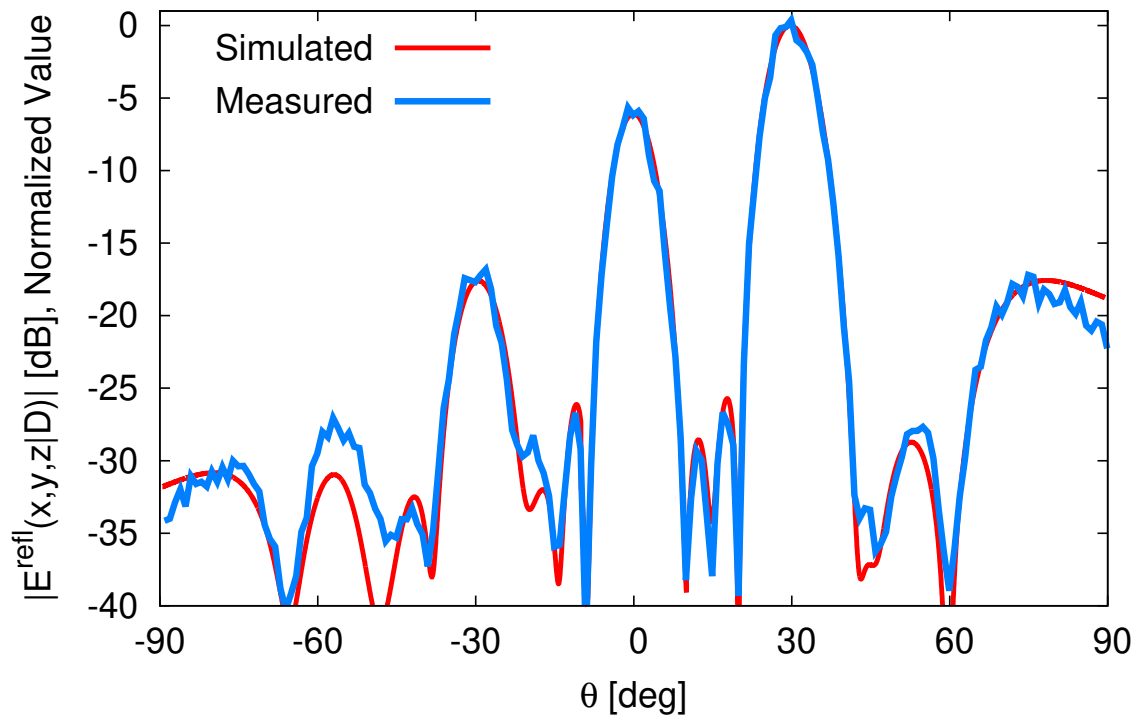


(a)



(b)

$(\theta^{\text{refl}}, \phi^{\text{refl}}) = (30, -45)$ [deg], $\phi = \phi^{\text{refl}}$, $P \times Q = 15 \times 15$, D^{opt}



(c)

Fig. 15 - G. Oliveri et al., “On the Improvement of the Performance of ...”